https://doi.org/10.5194/egusphere-2026-493
Preprint. Discussion started: 2 March 2026

Long-term Climatology of Vertical Profiles of Polarimetric Variables and Ice-microphysical Retrievals at X-band. Part I: Radar Calibration

Tobias Scharbach[1] and Silke Trömel[1, 2]

[1]Institute of Geosciences, Department of Meteorology, University of Bonn, Bonn, Germany
[2]Laboratory for Clouds and Precipitation Exploration, Geoverbund ABC/J, Bonn, Germany

Correspondence: Tobias Scharbach (toscha@uni-bonn.de)

Abstract. In a two-part series of papers, a climatology of quasi-vertical profiles (QVPs) of polarimetric variables and ice-microphysical retrievals such as ice water content, total number concentration and mean volume diameter is presented. QVPs are generated from plan position indicator scans at 18° elevation angle measured with the X-band radar located in the city of Bonn in western Germany between 2013 and 2023. They have been statistically analysed including error analysis with special emphasis on the characteristics of the melting layer and the dendritic growth layer. This long-term climatology improves the understanding of microphysical processes in stratiform cloud regimes and provides a reference for numerical weather prediction modellers to e.g. advance existing microphysical bulk paramerisation schemes.

While part two analyses and discusses the climatology, this first part of the series describes the prior thorough calibration of the radar reflectivity factor (Z_H) and the differential reflectivity (Z_{DR}). One method uses the relation between Z_H and Z_{DR} in light rain to calibrate Z_H. Best fits are determined from simulated Z_H and Z_{DR} values obtained with T-matrix calculations for various temperatures and values of the width of the canting angle distribution using a large disdrometer dataset of drop size distributions measured over Germany (mostly Bonn). Since this Z_H calibration technique strongly depends on the accuracy of Z_{DR} and encountered deficiencies in the birdbath scan, QVPs in light rain have been used to calibrate Z_{DR}. Obtained Z_H offset values are validated and compared using both satellite information and self-consistency relationships including specific differential phase (K_{DP}). The successful calibration of Z_H is confirmed by the root-mean-square error (0.70 dBZ), the mean-absolute error (0.60 dBZ), and the mean-bias (-0.50 dBZ) compared to the offsets obtained from satellite information. Offsets calculated by applying self-consistency relations show larger discrepancies, which favours the suitability of the novel method.

https://doi.org/10.5194/egusphere-2026-493
Preprint. Discussion started: 2 March 2026

1 Introduction

Numerical weather prediction (NWP) models generally struggle with limitations of existing parameterisation schemes to adequately capture the complexity of microphysical processes (Ryzhkov et al., 2020; Fan et al., 2017). Since polarimetric radars enable us to distinguish between hydrometeors with different microphysical properties and/or habits (e.g. shape and number concentration) and to identify so-called polarimetric fingerprints indicating ongoing dominating microphysical processes like e.g. aggregation, size sorting or dendritic growth (Ryzhkov et al., 2016; Trömel et al., 2019; Kumjian, 2013a; Kumjian and Ryzhkov, 2010, among others), they can serve as a powerful tool for improving NWP parameterisation schemes and cloud models (Kennedy and Rutledge, 2011; Ryzhkov et al., 2020). The fusion of radar polarimetry and atmospheric modelling is a promising pathway to improve the representation of clouds and precipitation in NWP (Trömel et al., 2021). Using observation-(forward) operators (Kumjian and Ryzhkov, 2012; Ryzhkov et al., 2020), such as the Efficient Modular VOlume scan RADar Operator (EMVORADO; Zeng et al., 2016; Blahak, 2016; Blahak and de Lozar, 2021), synthetic polarimetric variables can be calculated from simulated hydrometeor mass fractions and number concentrations of NWP models and directly compared with observed polarimetric variables (e.g. on the radar grid; Trömel et al., 2023; Shrestha et al., 2022; Xie et al., 2021). E.g., with a detailed model evaluation in radar observation space, Shrestha et al. (2022) identified excessive graupel production in the COnsortium for Small scale MOdeling (COSMO) model (Doms and Baldauf, 2018; Doms et al., 2018) with the Seifert-Beheng two-moment microphysical parameterisation (SB2MP) scheme (Seifert and Beheng, 2006). To date, extensive graupel formation is still an ongoing challenge in many microphysical paramerisation schemes. Furthermore, model evaluation studies in radar observation space as well as polarimetric microphysical retrievals and in-situ observations show that existing NWP models coupled with various microphysical schemes tend to overestimate the size of aggregates and underestimate the number concentration of ice particles in general (e.g.; Fridlind et al., 2017; Ori et al., 2020; Trömel et al., 2023, among others). Besides case studies, climatologies of polarimetric variables and microphysical retrievals are particularly important and serve as a statistically significant reference to understand and finally improve precipitation processes in atmospheric models.

In order to provide the required reliable information to NWP modelers, but also for most other radar applications in the scientific community and operational services, like quantitative precipitation estimation (QPE), nowcasting, hydrometeor classification and microphysical retrievals, precise calibration is a mandatory prerequisite (e.g. Ryzhkov and Zrnić, 2019; Warren et al., 2020; Houze Jr et al., 2004; Crisologo, 2019). Although the use of novel gradient approaches (e.g. Planat et al., 2021) and phase-based measurements are gaining increased attention and popularity, it is unlikely that absolute values of the reflectivity factor Z_H and differential reflectivity Z_{DR} will ever become superfluous and instead will always remain a part of hybrid QPE and microphysical retrieval derivations. Calibration is also (even maybe to a lesser extent) relevant for climatologies in order to represent reality with sufficient accuracy and statistical significance by minimizing calibration induced uncertainties as much as possible. Over the years, many techniques for calibrating Z_H and Z_{DR} have been developed and applied. Examples are the use of disdrometer data (e.g. Frech et al., 2017; Schneebeli et al., 2024; Frech, 2013), corner reflectors or metal spheres (attached on e.g. drones and balloons; e.g. Atlas and Mossop, 1960; Atlas, 2002; Williams et al., 2013; Ye et al., 2024), virtually

https://doi.org/10.5194/egusphere-2026-493
Preprint. Discussion started: 2 March 2026

generated radar targets (Schneebeli et al., 2024), solar signals (e.g. Frech and Hubbert, 2020; Holleman et al., 2010; Chu et al., 2019), stable ground clutter signals (e.g. Silberstein et al., 2008; Wolff et al., 2015; Pejcic et al., 2022; Hunzinger et al., 2020) or dominant point targets located close to the radar site (Gabella, 2018), self-consistency relations of polarimetric variables (e.g. Gorgucci et al., 1992; Louf et al., 2019; Gourley et al., 2009), Z_H-Z_{DR} dependencies in light rain (e.g. Ryzhkov and Zrnić, 2019), satellite (spaceborn) radar information (Pejcic et al., 2022; Louf et al., 2019; Louf and Protat, 2023; Crisologo et al., 2018), quasi-vertical profiles (QVPs; Ryzhkov et al., 2016) in light rain (Sanchez-Rivas and Rico-Ramirez, 2022), dry aggregated snow (e.g. Hu et al., 2024; Ryzhkov et al., 2005; Zittel et al., 2014), clear air Bragg scattering (e.g. Richardson et al., 2017), or the so-called birdbath scan method (e.g. Frech and Hubbert, 2020; Louf et al., 2019; Ryzhkov and Zrnić, 2019; Pejcic et al., 2022; Sanchez-Rivas and Rico-Ramirez, 2022). The latter is one of the most frequently used methods for accurate calibration of Z_{DR}, however, not all radars are mechanically designed to perform a 90° scan.

The first part of the paper series focuses on the prior, as noted above, very important calibration of Z_{DR} and Z_H, while the second part deals with the description and the statistical analysis of the climatology of QVPs of polarimetric variables and ice-microphysical retrievals obtained from 10 years of X-band radar data measured in stratiform rain. One major benefit and motivation using the QVP technique for the climatology is the reduction of statistical errors of polarimetric variables and microphysical retrievals when calculating the mean or median over the azimuth dimension in PPI scans (e.g. Tobin and Kumjian, 2017; Trömel et al., 2019, 2014).

Most of the calibration methods briefly presented above are either not retrospectively applicable because e.g. the required scanning strategy is missing, the radar system is simply not capable of setting it up, or it is not possible to cover the whole time period. Although the birdbath method is widely used to calibrate Z_{DR}, the results were not reliable for the whole period of the climatology. Instead a modified method adapted from Sanchez-Rivas and Rico-Ramirez (2022) using QVPs in light rain is exploited for Z_{DR} calibration and a Z_H calibration technique applicable to the entire time series from 2013 to 2023 is presented. It uses the known Z_H-Z_{DR} dependency (Ryzhkov and Zrnić, 2019), but with Z_{DR} as a predictor for Z_H measured on PPI scans at 18° elevation angle. This calibration method of Z_H is validated and compared to Z_H offset values obtained from satellite measurements, provided for a 5.5 year subset by Pejcic et al. (2022) and self-consistency relations as described in e.g. Louf et al. (2019).

The paper is structured as follows: Section 2 shortly introduces most important technical information and scanning strategies of the used radar and describes the steps of phase processing in more detail. The following Sect. 3 explains the problems encountered when using the birdbath scan method to correct Z_{DR} and presents the above mentioned alternative Z_{DR} calibration method used in this study, followed by the novel Z_H calibration method, its validation and the comparison with the self-consistency relation. Section 4 summarises the results, highlights deficiencies and identifies potential improvements for future studies.

https://doi.org/10.5194/egusphere-2026-493
Preprint. Discussion started: 2 March 2026

2 Radar data

The radar data used in this study have been obtained with the polarimetric X-band radar in Bonn, Germany (BoXPol), located at 50.7305° N and 7.0717° E and 99.5 m above mean sea level (MSL). BoXPol measures within a radius of 100 km since 2010 (Fig. 1). The radar operates in the simultaneous transmit and receive of horizontal and vertical polarized electromagnetic (EM) -waves (STAR) mode (Ryzhkov and Zrnić, 2019) using an Enigma signal processor. Plan position indicator (PPI) scans are generated at 10 different elevation angles, ranging from 1° to 28° and a (90°) birdbath scan in 5 min temporal and 1° azimuthal resolution. The range resolution depends on the chosen configuration of the elevation scan and ranges from 25 m to 150 m. For the 18° elevation angle (used in this two paper series) it is 100 m until the third of April 2017 and afterwards 125 m, where Enigma 3 was updated to Enigma 4. BoXPol operates in dual pulse repetition frequency (PRF) unfolding (staggering) mode 3, with alternating low and high PRF values in the azimuth dimension and varying high PRF values from 400 to 1150 Hz for the range resolution (personal communication with Kai Mühlbauer[1], see also Table 1). A range height indicator (RHI) scan is included in a 5 min scan schedule as well. For a more detailed information about the scanning strategies, reference is made to Diederich et al. (2015) or Pejcic et al. (2022).

All offset values (Z_{DR} and Z_H) are determined using PPI scans at 18° elevation angle. These measurements are also used in Part 2 of this paper series for the climatology. The choice of this elevation angle represents a compromise: It already provides sufficient vertical profile information, but the use of even higher elevation angles would result in a significant degradation of the polarimetric information content. At angles below 20°, however, only slight acceptable decreases occur (Ryzhkov et al., 2005; Griffin et al., 2018; Trömel et al., 2019).

For the calibration of Z_H and Z_{DR} only data with a cross-correlation coefficient (ρ_{HV}) ≥ 0.7 is used to mitigate possible non-meteorological contamination and clutter effects. Within the phase processing, first the system phase offset (ϕ_{DP}^{sys}; Ryzhkov and Zrnić, 2019) has to be determined and subtracted from ϕ_{DP}. ϕ_{DP}^{sys} is calculated by filtering with $\rho_{HV} \geq 0.9$ and $Z_H \geq 0$ and identifying the position of the first non-NaN measurement of ϕ_{DP} in each ray. Subsequently, the median of the values between this position and 3 km in the range dimension provide ϕ_{DP}^{sys}.

Afterwards, the offset-corrected ϕ_{DP} is smoothed using a moving median with a window length of 11 range bins. The specific differential phase (K_{DP}; e.g. Trömel et al., 2014; Ryzhkov and Zrnić, 2019; Vulpiani et al., 2012) in degrees per kilometer (°km^{-1}) is calculated applying low-noise Lanczos differentials (Holoborodko, 2015) implemented in the python module *wradlib*, using a window length of 31 range bins (corresponding to 3.1-km slant range for Enigma 3 and 3.875 km slant range for Enigma 4).

[1]Further information is available in the GAMIC Enigma 3 manual.

https://doi.org/10.5194/egusphere-2026-493
Preprint. Discussion started: 2 March 2026

Table 1. Technical description of the X-band radar in Bonn (BoXPol).

Parameter	**BoXPol**
Radar type	Dual-Pol X-band radar
Longitude	7.0717° E
Latitude	50.7305° N
Altitude	99.5 m
Wavelength (λ)	3.2 cm
Frequency	9.3 GHz
3-dB antenna beamwidth	~1°
Signal processor	GAMIC Enigma 3 to 3 April 2017, thereafter Enigma 4
Transmit type	STAR
Temporal resolution	5 min
Radial resolution	25 m to 200 m
Elevation angles	1° to 28° with 90° (birdbath scan)
Azimuth dimension	1° to 360°
Mode	Pulse staggering
High PRF	400 Hz to 1150 Hz
Pulse duration (τ)	0.2μs

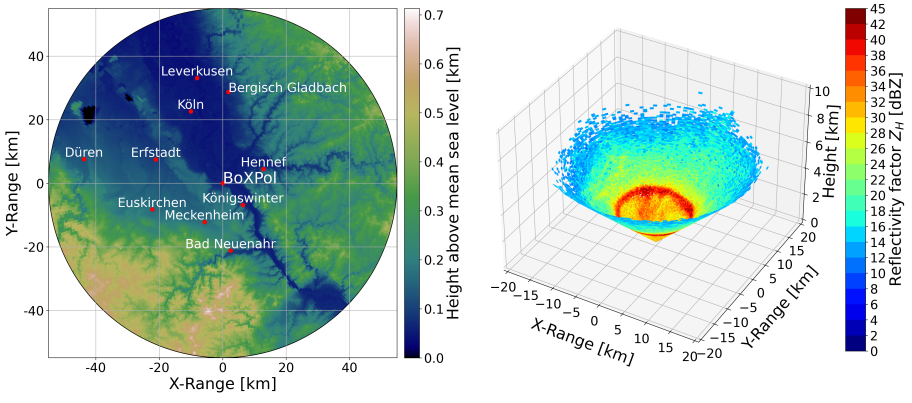

Figure 1. Location of BoXPol and covering area of the PPI scans at 18° elevation angle (550 km maximum range) including terrain height information and city names in the surrounding region given as red points (left). Example illustration of Z_H in a cone of the 18° PPI scan at the 7 October 2014, 00:00 UTC (right). Note that this figure represents the maximum range of BoXPol operating with Enigma 3 until the 4 March 2017.

https://doi.org/10.5194/egusphere-2026-493
Preprint. Discussion started: 2 March 2026

Table 2. Logbook of BoXPol displaying most important changes in hardware and software in the time period from January 2013 to March 2023.

Date	Important changes of BoXPol
2013	No important notifications
04.24.2014	Restart of radar (due to system failures)
04.03.2017	Enigma 3 to Enigma 4 software change
04.27.2017 to 04.28.2017	Change of Magnetron (receiving channel calibration)
06.14.2019	Shutdown complete system
07.26.2020	Restart of radar
01.30.2021 to 01.31.2021	Radar breakdown
07.03.2021	Restart of radar
01.10.2021 to 01.12.2021	Magnetron errors and/or other issues
05.30.2022	Change of Magnetron (receiving channel calibration)
03.09.2023	Last shutdown of radar (Broken Magnetron)

3 Calibration of Z_{DR} and Z_H

Assuming no specific attenuation (A_H; e.g. Kumjian, 2013b), wet radome effects (e.g. Le Loh et al., 2022) or noise influences (e.g. Schneebeli et al., 2024), a simple representation of the measured Z_H (e.g. Silberstein et al., 2008; Louf and Protat, 2023) based on the well-known radar equation (e.g. Ryzhkov and Zrnić, 2019; Doviak et al., 1994; Rinehart, 1997), can be used to characterize possible calibration errors with the following equation:

$$Z_H = -10\log_{10}\underbrace{\left(\frac{\pi^3\,|K_w|^2}{\lambda^2\cdot 1024\cdot \ln 2\cdot 10^{18}}\,P_t^H\left(G^H\right)^2\theta_h^H\theta_v^H c\tau A_t^H A_r^H\right)}_{C_r^H} + 20\log_{10} r + 10\log_{10} P_r^H. \tag{1}$$

P_r^H is the received and P_t^H the transmitted power of the horizontal polarization channel in W, K_W is the dielectric factor of water, θ_h^H and θ_V^H are the antenna beam widths of the two orthogonal directions of the horizontal channel in radians, c is the speed of light in ms^{-1}, G^H is the antenna gain of the horizontal polarization channel with the assumption that the antenna is for both receiving and transmitting, A_t and A_r are the transmitter and the receiver gains of the horizontal polarization channel, τ is the pulse duration of transmitted signals in s and r is the radial distance of the target in m. Note that in Eq. 1 the power measurements are made at a reference plane directly behind the radar antenna and therefore no receiver or transmitter losses are considered (Schneebeli et al., 2024). The underbraced term in Eq. 1 is the so-called radar constant of the horizontal channel C_r^H (e.g. Schneebeli et al., 2024; Ryzhkov and Zrnić, 2019), which can vary over time and due to degradation of radar hardware (e.g. Louf et al., 2019) and represents the main source of potential calibration errors. Similarly, Eq. 1 is valid for the reflectivity factor of the vertically polarized EM wave (Z_V) in the STAR mode, i.e. superscripts and subscripts 'H' can be replaced by 'V'

https://doi.org/10.5194/egusphere-2026-493
Preprint. Discussion started: 2 March 2026

(e.g. Ryzhkov and Zrnić, 2019; Schneebeli et al., 2024). As a result, any difference in the radar constants for both polarization channels may also result in a Z_{DR} miscalibration, as illustrated by the following equation:

$$Z_{DR} = 10\log_{10}\left(\frac{P_r^H \cdot C_r^H}{P_r^V \cdot C_r^V}\right). \tag{2}$$

In the case of a perfectly calibrated (fictitious) radar (e.g. for the transmitter channel, for the receiver channel and for the antenna; Schneebeli et al., 2024), $C_r^H = C_r^V$ and thus, Z_{DR} depends on P_r^V and P_r^H only (e.g. Ryzhkov and Zrnić, 2019). Since a perfect internal calibration for the estimation of C_r is almost impossible, external sources/methods are mandatory for a sufficient calibration of Z_H and/or Z_{DR}[2] (Louf et al., 2019).

To enable quantitative applications like Quantitative Precipitation Estimation (QPE), microphysical retrievals or hydrometeor classification, Z_{DR} needs to be calibrated with an accuracy of 0.1 to 0.2 dB (Frech and Hubbert, 2020; Ryzhkov and Zrnić, 2019). As mentioned before, the birdbath (90° elevation angle) scan method is one of the most powerful calibration methods for Z_{DR} (Ryzhkov and Zrnić, 2019; Frech et al., 2017; Louf et al., 2019). Since the mean angle of incidence of small raindrops is close to 0°, they appear spherical when viewed from below. This means that both Z_H and Z_V should be equal and deviations can be used for calibration of Z_{DR} in light rain (Ryzhkov and Zrnić, 2019). In this study, Z_{DR} offsets from the birdbath scan are calculated using a similar but slightly more rigorous procedure compared to Pejcic et al. (2022). First, mixed phase hydrometeors are excluded using only data at heights at least 250 m away from the 0 °C isotherm. The temperature information is taken from the European Center for Medium-Range Weather Forecasts Reanalysis v5 (ERA5; Hersbach et al., 2020). Afterwards, the median between the 20th and 80th percentiles of Z_{DR} is calculated (instead of the 10th and 90th percentiles in Pejcic et al., 2022), whereby only days with > 100 non-NaN values and a standard deviation < 0.2 dB are considered as reliable for estimating the daily Z_{DR} offset.

However, serious inconsistencies in the Z_{DR} offset values obtained using the birdbath scan method were discovered. While the method provided reliable offsets for the period between April 2014 and March 2017, inaccuracies of more than 0.2 dB were obtained for other times. Due to various hardware and software changes between 2013 and 2023 documented in the BoXPol logbook (private communication with Kai Mühlbauer and Martin Lennefer, summarized in Table 2), such as the replacement of hardware components (e.g. Magnetron), software updates (Enigma 3 to Enigma 4), but also unfathomable influences, offsets derived from the birdbath scan seem not to be applicable to the 18° elevation PPI. These circumstances most likely lead to discrepancies in the components of C_r for both channels (see Eq. 2) and also may point to a potentially unsuspected elevation dependence. The latter could simply be related to the mechanically driven mechanism of BoXPol that adjusts the specific elevation angles in the scanning strategy (private communication with Martin Lennefer and Kai Mühlbauer). Therefore, the QVPs themselves are used to calculate the Z_{DR} offset (Sanchez-Rivas and Rico-Ramirez, 2022) and to subsequently calibrate Z_H based on the offset corrected Z_{DR}.

In the following, Sect. 3.1 describes the Z_{DR} calibration technique and Sect. 3.2 the calibration of Z_H, while Sect. 3.2.1 and Sect. 3.2.2 compare and validate the results using self-consistency relations and satellite information.

[2]Some of these techniques are briefly mentioned above.

https://doi.org/10.5194/egusphere-2026-493
Preprint. Discussion started: 2 March 2026

3.1 Z_{DR} Calibration

Light rain conditions are identified with $0 < Z_H < 20$ dBZ and $\rho_{HV} > 0.985$ (Sanchez-Rivas and Rico-Ramirez, 2022) and ϕ_{DP} <30° to exclude regions with strong attenuation. To ensure that the calculation includes liquid hydrometeors exclusively, only data at least 250 m below the height of the 0 °C isotherm is used. QVPs are only computed if there are at least 100 valid values in the azimuth dimension. Subsequently, only QVPs with at least 10 valid values in the height dimension are included in the overall calculation of the daily Z_{DR} offset. The mean value of each QVP (calculated over the height dimension) subtracted by the expected simulated average value of Z_{DR} for the range between 0 and 20 dBZ (light rain) defines the offset value of Z_{DR} (Z_{DR}^{off}). To determine the expected Z_{DR} value, T-matrix simulations (Waterman, 1971) are performed based on drop-size distributions (DSDs) measured with a Thies disdrometer on the rooftop of the Institute for Geosciences, Department of Meteorology, University of Bonn, Germany, between November 2011 and December 2019, and with 68 Thies disdrometers of DWD during 30 rainy days between 2015 and 2017. More detailed information on the processing of this disdrometer dataset can be found in Chen et al. (2021). T-matrix simulated Z_H and Z_{DR} values at X-band (λ =3.2 cm) and 18° elevation angles are obtained using properties of homogeneous non-spherical scatterers assuming a 2D axisymmetric Gaussian distribution of orientations for oblate hydrometeors (Ryzhkov et al., 2011; Ryzhkov and Zrnić, 2019) with 0° mean canting angle and the raindrop shape model following Brandes et al. (2002). Figure 2 presents the 2D-distribution of Z_{DR} and Z_H for the width of the canting angle distribution (std(C)) of 8° at 10 °C.

Only small differences in average simulated Z_{DR} in light rain ($\overline{Z_{DR}^{T-sim}}$) and best-fit lines of $Z_{DR} = f(Z_H)$ for different temperatures between 5 and 30 °C in Fig. 2 demonstrate that temperature dependencies can be neglected. Thus, $\overline{Z_{DR}^{T-sim}} = 0.1$ dB is determined as the intrinsic Z_{DR} value in light rain for X-band radar data at elevation angles of 18°. Results are in agreement with Sanchez-Rivas and Rico-Ramirez (2022) (their Fig. 4 (a)).

Finally, the median of a day's Z_{DR}^{off} values (med[Z_{DR}^{off}]) gives the daily Z_{DR} offset. Daily offsets are only calculated if the standard deviation of Z_{DR}^{off} is < 0.2 dB with at least > 100 valid values. Days without defined offset are filled with a centered 30 day rolling mean of med[Z_{DR}^{off}]. Note, daily Z_{DR} offsets have to be subtracted from the measured Z_{DR} of the PPI scans.

Z_{DR} offsets derived from the birdbath scan calculated following Pejcic et al. (2022) but with a stricter filtering using only data between 20th and 80th percentile (instead of 10th and 90th percentile) are now compared with the ones obtained with the modified QVP method for the period from June 2014 to April 2017. Therefore, the same gap-filling procedure as described above is applied to the birdbath scan Z_{DR} offset values. E.g., on 1 January 2013 the offset values obtained with the two methods show a relatively large difference of 0.18 dB (Fig. 4). Negative Z_{DR} values (less than -0.1 dB) directly above the ML together with even more negative values of up to -1 dB in the liquid phase (panel (c)) indicate that the offset derived with the birdbath method is not adequate for the 18° scan. The Z_{DR} offset time series obtained with the two methods for the time period from January 2013 to March 2023 show similar trends, but deviations of about 0.2 dB or more occur in the period from 2013 to April 2014 and from April 2017 to June 2019 (Fig. 5). Another period of larger deviations is seen around December 2021 to June 2022. Differences between the two methods are most likely associated with changes of the Magnetron (accompanied by receiving channel calibrations), the software change from Enigma 3 to Enigma 4 and general restarts of the radar after system

https://doi.org/10.5194/egusphere-2026-493
Preprint. Discussion started: 2 March 2026

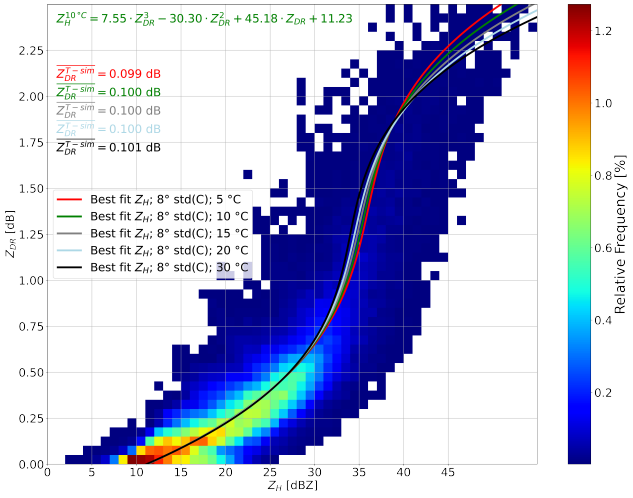

Figure 2. Z_H-Z_{DR} relationship based on T-matrix scattering simulations at 18° elevation angle and 10 °C using disdrometer measurements between November 2011 and December 2019 on the roof of the Institute for Geosciences, Department of Meteorology, University of Bonn, and 30 rain days between 2015 and 2017 from 68 Thies disdrometers of DWD (Chen et al., 2021). The best-fit lines of simulated Z_{DR}=f(Z_H) for different temperatures are indicated in different colors including the according inverted equation Z_H=f(Z_{DR}) (in green) achieved for 10 °C and std(C) of 8° used for Z_H calibration (see also Eq. 3). The mean values of Z_{DR} between 0 and 20 dBZ ($\overline{Z_{DR}^{T-sim}}$) for the different temperatures are also given.

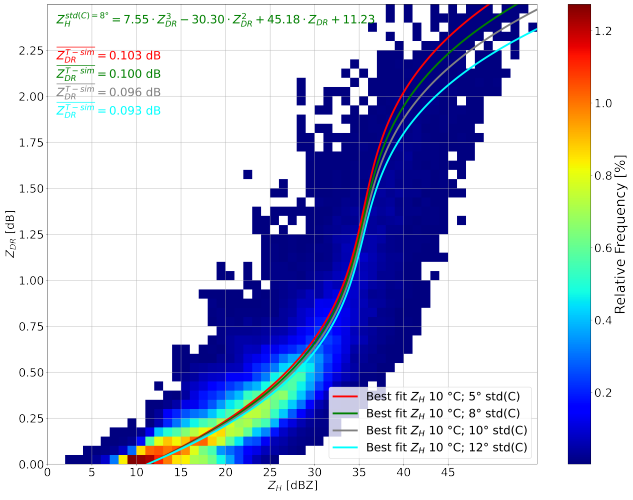

Figure 3. As in Fig. 2 but the best-fit lines of simulated $Z_{DR} = f(Z_H)$ at a constant temperature of 10 °C with various std(C) and the mean values of Z_{DR} between 0 and 20 dBZ ($\overline{Z_{DR}^{T-sim}}$) for different std(C) values.

failures. Within the stable period from 24 April 2014 to 3 April 2017, however, the Z_{DR} offsets of the two methods are very

https://doi.org/10.5194/egusphere-2026-493
Preprint. Discussion started: 2 March 2026

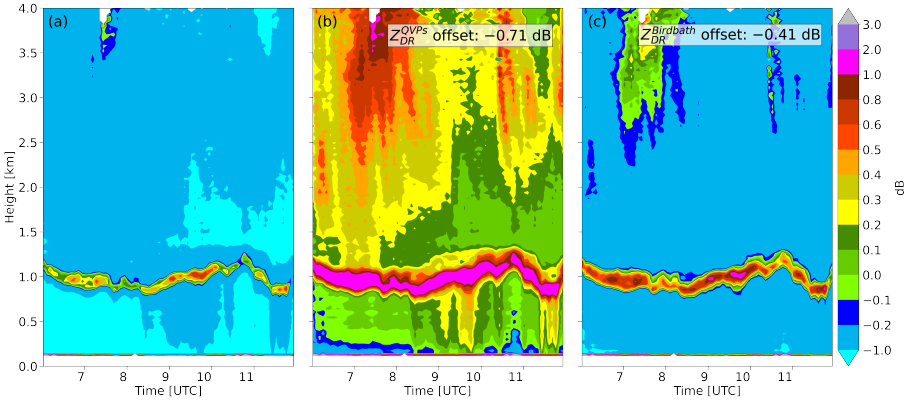

Figure 4. QVPs of Z_{DR} not offset corrected (a), offset corrected using QVP method (b) and birdbath scan method (c) for the 1 January 2013, from 06:00 UTC to 12:00 UTC.

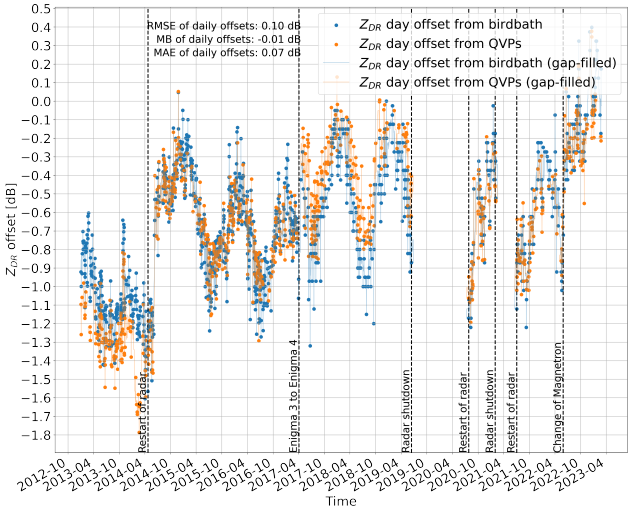

Figure 5. Daily Z_{DR} offsets calculated using for the period between January 2013 to March 2023 the QVP (orange) and birdbath scan (blue) method, respectively. The times of important changes in BoXPol are given as vertical dashed lines with the respective caption. RMSE, MB and MAE calculated for the time period between 24 April 2014 and 3 April 2017 are shown as well.

close to each other. This is confirmed by a root-mean-square error (RMSE) of 0.1 dB, a mean-absolute error (MAE) of 0.07 dB and the mean-bias[3] (MB) of -0.01 dB (e.g. Von Storch and Zwiers, 2002).

[3]The mean-bias is the mean value between the difference of the 30 day rolling mean gap-filled Z_{DR} offset obtained from the birdbath scan and from QVPs.

https://doi.org/10.5194/egusphere-2026-493
Preprint. Discussion started: 2 March 2026

3.2 Z_H calibration using the Z_H-Z_{DR} relationship

In the next step Z_H is calibrated exploiting the Z_H-Z_{DR} relationship (e.g. Ryzhkov and Zrnić, 2019) but with Z_{DR} as a predictor for Z_H on PPIs at 18° elevation angles. In the following the method will be referred to as the reverse Z_H-Z_{DR} method, since, to the authors' knowledge, it has so far only been used to calibrate Z_{DR}.

Again, mixed or solid phase hydrometers are excluded by focusing on data at least 250 m below the height of the 0 °C isotherm taken from the ERA5 data set. Unlike for the Z_{DR} calibration, PPIs instead of QVPs are used and are filtered with $\rho_{HV} > 0.99$ and $\phi_{DP} < 30°$. Like for the Z_{DR} calibration at least 100 non-NaN values are required along the azimuth dimension to be taken into account. Additionally, at least two thirds of the valid Z_H bins of a PPI must show a valid Z_{DR} value. Only days with at least 10 PPIs per day, each with at least 100 valid values, are used for further calculation. Each PPI with a Spearman correlation coefficient $corr_{spear} < 0.4$ is excluded from further calculations of the daily Z_H offset. Here, $corr_{spear}$ is calculated based on the positive Z_H and Z_{DR} values and is used because of possible deviations from the Gaussian, non-linearities and reduced sensitivity to outliers compared to the Pearson correlation coefficient. Finally, the simulated Z_H-Z_{DR} dependency (Fig. 2) provides the expected Z_H (Z_H^{ideal}) per day based on the Z_{DR} values of the filtered PPIs. More precisely, the best fit of simulated Z_H at 10 °C with std(C) equals 8° is used:

$$Z_H^{ideal} = 7.55 \cdot Z_{DR}^3 - 30.30 \cdot Z_{DR}^2 + 45.18 \cdot Z_{DR} + 11.23. \quad (3)$$

As outlined before, variations with temperature are neglectable for $Z_{DR} < 2$ dB (Fig. 2) and the temperature chosen is roughly the average annual temperature in Germany. Similarly, changing the std(C) in the range from 5°C to 12°C has only minor influence (Fig. 3). The expected Z_H^{ideal} is subtracted from the measured Z_H to obtain the calibration offset of a PPI ($Z_H^{off} = Z_H - Z_H^{ideal}$). Again, only values between the 20th and 80th percentile of Z_H^{off} and with a standard deviation of $Z_H^{off} < 4$ dBZ are considered to derive the daily offset. These thresholds have been chosen based on rough visual impressions of the daily standard deviations of the GPM derived Z_H offsets in Pejcic et al. (2022), Louf and Protat (2023) and Protat et al. (2022) (their Fig. 2, Fig. 12 and Fig. 2, respectively).

Finally, calculating the median of these filtered Z_H^{off} (med[Z_H^{off}]) gives the daily Z_H offset. Using the median instead of the mean reduces the impact of outliers caused by e.g. size sorting effects. Consistent with the methodology for the calibration of Z_{DR}, any gaps in the time series of med [Z_H^{off}] are filled using a rolling mean of 30 days. Offsets are defined to be subtracted from the measured Z_H values to obtain the offset-corrected Z_H. As an example, Fig. 6 demonstrates the performance of the method, i.e. the offset-corrected Z_H-Z_{DR} distribution is shifted towards the ideal simulated Z_H-Z_{DR} curve. QVPs of Z_H show the more pronounced bright band and aggregation signature (Fig. 4 and 7), whereby the higher values of Z_H after offset correction appear to be more realistic.

3.2.1 Validation of Z_H-calibration using the self-consistency relationship

The relationship between the ratio $K_{DP}Z_h^{-1}$, with the reflectivity factor in linear scale ($Z_h = 10^{0.1Z_H}$) in (mm^6 m^{-3}), and Z_{DR} in rain (e.g. Gorgucci et al., 2006) represents an alternative opportunity to calibrate radars (e.g. Marks et al., 2011).

https://doi.org/10.5194/egusphere-2026-493
Preprint. Discussion started: 2 March 2026

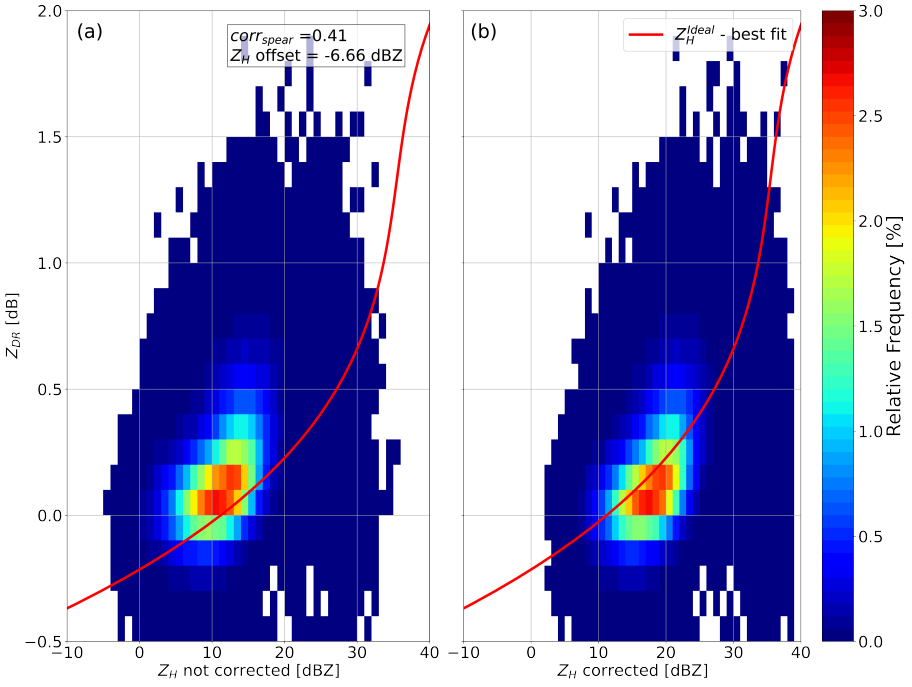

Figure 6. 2D histogram of offset corrected Z_{DR} versus Z_H not offset corrected (a) and offset corrected (b) for the 1 January 2013, using the proposed reverse Z_H-Z_{DR} method. The thick red line indicates the calculated ideal (best fit) Z_H (Z_H^{ideal}) (Eq. 3).

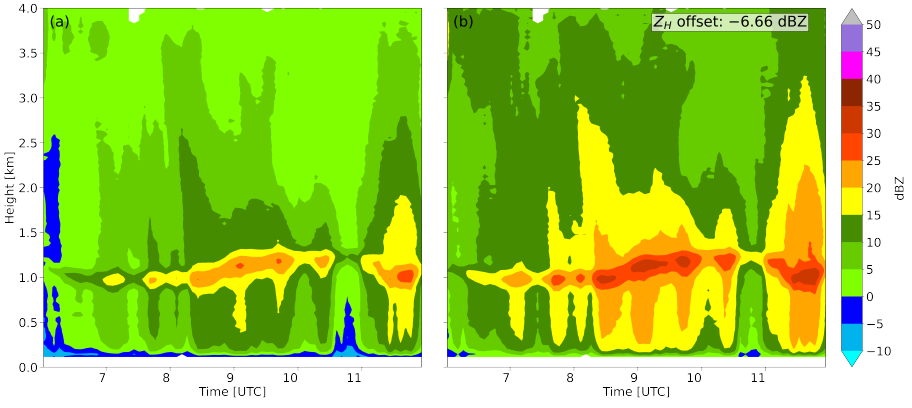

Figure 7. QVPs of (a) uncorrected and (b) corrected Z_H using the reverse Z_H-Z_{DR} method for the 1 January 2013, from 06:00 UTC to 12:00 UTC.

This technique is often utilized to calibrate Z_H of operational radars because, similar to the Z_H-Z_{DR} relationship, it does not require comparative analysis, e.g. with other technical devices or instruments (Lee et al., 2021). However, applying published self-consistency relationships derived in different geographical locations and climate regimes can lead to large discrepancies

https://doi.org/10.5194/egusphere-2026-493
Preprint. Discussion started: 2 March 2026

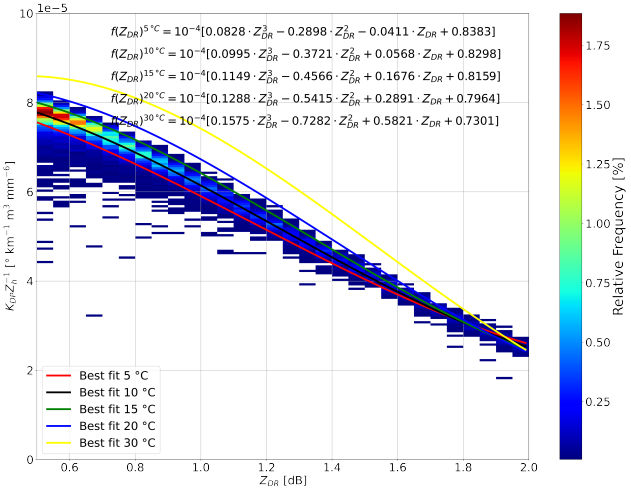

Figure 8. T-matrix simulated $(K_{DP}Z_h^{-1})$-Z_{DR} dependencies at 18° elevation angle and 10 °C based on disdrometer measurements for the period from November 2011 to December 2019 on the rooftop of the Institute for Geosciences, Department of Meteorology, University of Bonn, and 30 rainy days between 2015 and 2017 from 68 Thies disdrometers of the DWD (Chen et al., 2021). The best fit lines of the simulated $f(Z_{DR})$ for different temperatures are also given.

(Louf et al., 2019). Since the ratio $K_{DP}Z_h^{-1}$ is also temperature dependent at X-band (Ryzhkov and Zrnić, 2019), we derive a set of self-consistency relationships for Germany at various temperatures based on T-matrix simulated K_{DP}, Z_h and Z_{DR} using again the DSD dataset and the assumptions outlined in Sect. 3. Only DSDs with $0.5\ \text{dB} > Z_{DR} < 2\ \text{dB}$ (Louf et al., 2019) are considered to determine the resulting best-fit equations $f(Z_{DR})$ for the ratio $K_{DP}Z_h^{-1}$ as presented in Fig. 8. Subsequently we determine the expected Z_H, in the following referred to as Z_H^{self}, for comparison with the offset corrected Z_H using the reverse Z_H-Z_{DR} method, with the following equation:

$$Z_H^{self}(i) = 10\log_{10}\left(\frac{K_{DP}(i)}{f(Z_{DR})(i)}\right), \tag{4}$$

where the index i indicates the different equations for 5 °C, 10 °C, 15 °C, 20 °C and 30 °C, respectively. For an comparison in nearly homogeneous conditions, QVPs of stratiform rain events are generated, whereby in contrast to Sec.3.1, prior filtering combines the use of the ML detection algorithm by Wolfensberger et al. (2016) but modified for application to QVPs by Trömel et al. (2019) and the Shannon information entropy (see Appendix A, Trömel et al. (2023)). Filtering with the minimum Shannon information entropy $\min(\eta(X)_{norm}) \geq 0.85$ guarantees an increased degree of homogeneity in the PPI scans prior QVP generation. All QVP bins derived with the PPIs at 18° elevation monitored between 2013 and 2023 fulfilling these criteria are considered. The validation based on temperature information obtained from ERA5 further demonstrates the suitability of the stratiform filter technique (in particular the ML detection algorithm, see Appendix B). As above, following Louf et al. (2019) and Ryzhkov and Zrnić (2019), filtering with $0.5\ \text{dB} < Z_{DR} < 2\ \text{dB}$, SNR$> 25$ dB, $\rho_{HV} > 0.99$ and additionally $\phi_{DP} < 30°$ is applied to the QVPs (see Sec.3.1). Here, K_{DP} and offset-corrected Z_{DR} values of these QVPs are used to calculate Z_H^{self} using Eq. 4 and opposed to the offset-corrected Z_H of the QVPs. The comparison shows a moderate agreement, as indicated

https://doi.org/10.5194/egusphere-2026-493
Preprint. Discussion started: 2 March 2026

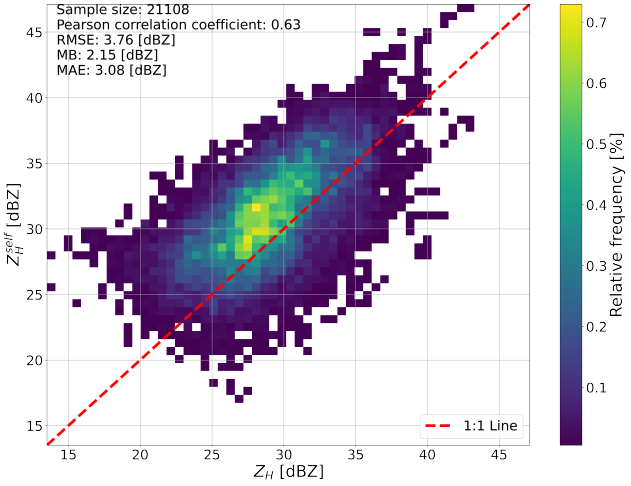

Figure 9. 2D histogram of Z_H^{self} (see Eq. 4) versus measured and offset corrected Z_H using the reverse Z_H-Z_{DR} method in the time period from 2013 to 2023. In addition to the sample size, Pearson correlation coefficient, RMSE, MB and MAE are also given.

by the correlation of 0.63 (Fig. 9). Additionally, the majority of Z_H^{self} values are larger than the measured Z_H, showing a MB[4] of 2.15 dBZ. The RMSE of 3.76 dBZ and the MAE of 3.08 dBZ confirm this observation.

Louf et al. (2019) show in their Fig. 15 the Z_H^{self} against calibrated Z_H obtained from the C-band polarimetric radar located near Darwin in northern Australia, using different raindrop shape models at 20 °C temperature and two different std(C). Overall, the distribution shown in Fig. 9 compares well with Fig. 15 in Louf et al. (2019), giving additional confidence also in using the 30-day rolling mean gap-filling procedure of the Z_H offsets. However, Fig. 9 shows higher values of Z_H^{self} and more outliers. Intrinsic uncertainties associated with the K_{DP} processing on the one hand, the temperature dependency, assumptions about the canting angle distribution and the chosen raindrop shape model in the T-matrix simulations on the other hand, may affect the results.

To gain more insight using self consistency Z_H calibration we additionally calculate Z_H offsets on a daily basis in a similar way as the Z_{DR} offsets (Sec. 3.1). In the following section, the two different Z_H offset calibration techniques are compared with each other and validated using satellite information.

3.2.2 Validation of Z_H-calibration using satellite information

Satellite measurements of the Dual-frequency Precipitation Radar (DPR) operating on the Global Precipitation Mission (GPM; e.g. Hou et al., 2014; Pejcic et al., 2020) core satellite are well suited for the calibration of ground based Z_H radar measurements as shown in e.g. Pejcic et al. (2022), Louf and Protat (2023), Louf et al. (2019), Warren et al. (2018) or Lee et al. (2021). Thus, Z_H offsets obtained in this study are compared with the ones calculated by Pejcic et al. (2022) in the period between 2014 and June 2019. Daily average Z_H offsets based on the differences between measurements of BoXPol and the satellite-based

[4]The mean-bias is the mean value between the difference of Z_H^{self} and the offset corrected Z_H using the reverse Z_H-Z_{DR} method.

https://doi.org/10.5194/egusphere-2026-493
Preprint. Discussion started: 2 March 2026

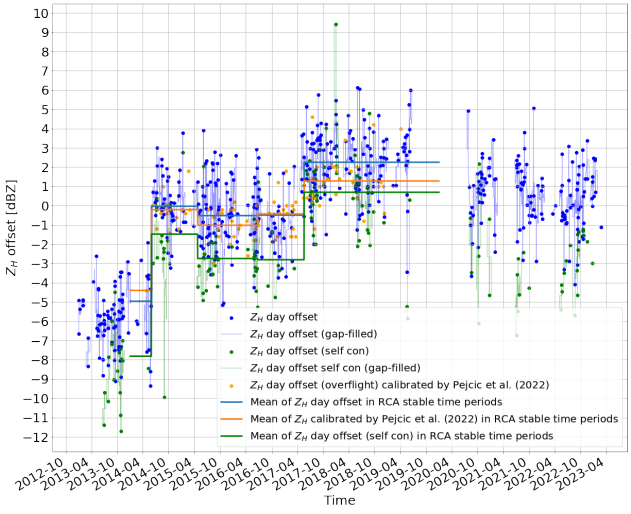

Figure 10. Daily Z_H offsets obtained from the reverse Z_H-Z_{DR} method (blue dots), the GPM overflights (orange dots; Pejcic et al., 2022) and the self-consistency relations ($\Delta_{self}[Z_H]$) in the period between January 2013 to March 2023, respectively. Mean values of Z_H offsets in RCA stable time periods from Pejcic et al. (2022) are given as blue, orange and green horizontal lines, respectively.

K_u-band radar (part of DPR, explained in more detail in Pejcic et al., 2022) are compared with daily offsets obtained using the reverse Z_H-Z_{DR} method and the self consistency relations (see Fig. 10). For the point-to-point comparison (nearest time of overflight and 30 day rolling mean gap filled Z_H offsets), both the RMSE of 1.88 dBZ and the MAE of 1.51 dBZ (MB[5] = -0.36 dBZ) are in an acceptable range but relatively high. The differing sample sizes (92 overflights of GPM), may explain part of the deviations. At the same time, however, this comparison demonstrates the applicability of the 30-day rolling mean to obtain a gap-filled time series of Z_H offsets. And even though the DPR itself has a calibration accuracy of less than $\pm$ 1 dBZ (Masaki et al., 2020; Warren et al., 2018), intrinsic uncertainties of $\approx$ 0.25 -0.5 dBZ for the K_u channel of the DPR must be considered in interpreting the accuracy of the reverse Z_H-Z_{DR} method (see for example Fig. 8 and 9 in Masaki et al., 2020). Furthermore, Pejcic et al. (2022) uses the mean value instead of the median for the respective days, which gives outliers more weight, potentially increasing the discrepancies between GPM derived Z_H offsets and med[Z_H^{off}]. RMSE and MAE improve only slightly without the 30 day rolling mean gap filled procedure (not shown). For the 30 day rolling mean gap filled Z_H offsets obtained from self-consistency relations, both the RMSE (2.23 dBZ) and the MAE (1.87 dBZ) are larger and offsets are more negatively biased compared to results obtained with the reverse Z_H-Z_{DR} method. The variabilities over the days, however, are rather similar for all three methods.

Additionally, the averaged satellite-derived Z_H offsets in stable calibration time periods identified with the relative calibration adjustment (RCA) technique (see Pejcic et al., 2022, for more information) are compared with according averaged values based on the 30-day rolling mean gap-filled Z_H offsets obtained from the reverse Z_H-Z_{DR} method and from the self-consistency

[5]The mean-bias is the mean value between the difference of the Z_H offsets obtained from GPM and the Z_H offsets obtained from the reverse Z_H-Z_{DR} method.

https://doi.org/10.5194/egusphere-2026-493
Preprint. Discussion started: 2 March 2026

Table 3. RMSE, MAE and MB for the 30-day rolling mean gap-filled Z_H offsets obtained using the reverse Z_H-Z_{DR} method and the self-consistency relations in comparison with GPM overflights (both also for the mean values in RCA stable time periods), as presented in Fig. 10.

	Z_H offsets (gap filled)	Z_H offsets (gap filled) in RCA stable time periods
RMSE [dBZ]	1.88	0.70
MAE [dBZ]	1.51	0.60
MB [dBZ]	-0.36	-0.50
	Z_H offsets (gap filled-self consistency)	Z_H offsets (gap filled-self consistency) in RCA stable time periods
RMSE [dBZ]	2.28	1.62
MAE [dBZ]	1.91	1.37
MB [dBZ]	1.14	1.37

relations (Fig. 8). The averaging of the offsets obtained from satellite information over this stable time periods reduces the uncertainties of the GPM derived offsets to less than 1 dBZ (e.g. Louf and Protat, 2023; Protat et al., 2022). Seasonal Variations triggered by e.g. changing vegetation (Louf and Protat, 2023) challenge the RCA method to identify stable time periods. Seasonal fluctuations are also recognisable in Pejcic et al. (2022) (their Fig. 2) and may have impacted the accuracy of the averaged Z_H offset value obtained from GPM overpasses in RCA stable time periods. Especially the stronger deviations between the averaged 30 day rolling mean gap filled Z_H offsets obtained by using the reverse Z_H-Z_{DR} method and the ones from the GPM overpasses in the last time period (2017-05-19 to 2019-06-30) are likely associated with these seasonal fluctuations. Nevertheless, both smaller RMSE and MAE strengthen confidence in using the reverse Z_H-Z_{DR} method instead of the self consistency relations (Table 3). In summary, since the self-consistency method bears several uncertainties and more confidence can be assigned to the comparison with satellite overflights, we conclude on the overall reliability of the reverse Z_H-Z_{DR} method for Z_H calibration.

4 Summary, discussion and outlook

The birdbath method, broadly used for Z_{DR} calibration, provided only for a limited time period (April 2014 to April 2017) of the BoXPol data set reliable results. Otherwise, inaccuracies of more than 0.2 dB have been detected. Instead, the approach by Sanchez-Rivas and Rico-Ramirez (2022) has been modified and applied successfully to ensure sufficient accuracy of Z_{DR} for the entire period (2013-2023).

This study aims to raise awareness of the need to critically use the birdbath method (or any other method based on one elevation scan only) and not apply the resulting offsets to the entire volume scan without further verification. Elevation dependent offsets

https://doi.org/10.5194/egusphere-2026-493
Preprint. Discussion started: 2 March 2026

have been identified already for other radars as well (e.g. Blanke et al., 2025). It may be necessary to calculate an individual Z_{DR} offset value for each of the elevations of interest, which can be time consuming and computationally expensive. Since accurately calibrated Z_{DR} values are key for applications such as QPE, HMC, or Z_H calibration exploiting the reverse Z_H-Z_{DR} method, further research is required to ensure reliable quantitative use of Z_{DR} in radar meteorology.

The reverse Z_H-Z_{DR} method has been validated and compared with satellite-based measurements and self-consistency relations. Z_H offsets derived with the reverse Z_H-Z_{DR} methodology agree well with the averaged Z_H offsets derived from GPM overpasses in stable RCA periods between 2014 and 2019 (Pejcic et al., 2022). Even a direct point-to-point comparison of daily Z_H offsets, which is critical due to the large difference in sample sizes, shows similar trends and acceptable RMSE and MAE values. To gain additional insights, expected Z_H values using self-consistency relations (Z_H^{self}) based on QVPs have been calculated as well. A stratiform filtering technique (see Trömel et al. (2023) and Appendix A) guarantees a sufficient degree of homogeneity for QVP generation. The comparison of Z_H^{self} and Z_H calibrated with the reverse Z_H-Z_{DR} method are consistent with results shown in Louf et al. (2019), with acceptable values for the RMSE, MAE and MB. In addition, the general overestimation of Z_H^{self} values is in agreement with the more negative daily derived Z_H offset values using self-consistency relations compared to the ones using the reverse Z_H-Z_{DR} method. The small number of outliers in Z_H^{self} can most likely be explained by uncertainties in K_{DP} derivations, DSD variability, temperature dependencies, assumptions on the canting angle distribution and the raindrop shape model used in the T-matrix simulations. The comparison between Z_H^{self} and the offset corrected Z_H using the reverse Z_H-Z_{DR} method gives confidence in the use of the 30-day rolling mean gap-filling procedure to adequately fill missing Z_H offset values.

In summary, we conclude on the overall reliability of the reverse Z_H-Z_{DR} method for Z_H calibration assuming a sufficiently accurate prior calibration of Z_{DR}. It may serve as a powerful alternative to standard Z_H calibration techniques like self-consistency relationships, and/or can be used, if satellite-based information for most accurate calibration of Z_H is missing. Regarding satellite-based calibration, seasonal variations and their impact on RCA stable time periods (Pejcic et al., 2022) could be addressed in the future by applying a dynamic clutter map (Louf and Protat, 2023) to reduce potential uncertainties in the GPM derived Z_H offset values.

Even though diurnal variations have been partially observed in the Z_{DR} offsets, this study aimed at daily Z_{DR} and Z_H offsets, deleting days with higher variability in the offset values (Z_{DR} offset standard deviation > 0.2 dB; Z_H offset standard deviation > 4 dBZ). However, calculations of temporally higher resolved offsets could potentially lead to more accurate estimates of offsets and especially reduce potential errors associated with the gap-filling method based on a 30-day rolling mean. To enable also the inclusion of e.g. sequences not fulfilling the filtering criteria for light rain, or even more intense convective events in the offset calculations, other Z_H-calibration methods, e.g. the one proposed by Diederich et al. (2015) using A_H, or methods combined in the integrated Satellite and Clutter Absolute Radar calibration (SCAR; Louf et al., 2019; Louf and Protat, 2023) scheme like solar calibration could be combined with the introduced reverse Z_H-Z_{DR} method. Further validation of the reverse Z_H-Z_{DR} method in different geographical/climatic regions and with an increased number of GPM overflights should be carried out in the future.

https://doi.org/10.5194/egusphere-2026-493
Preprint. Discussion started: 2 March 2026

Data availability. The ERA5 data is stored at the Climate Data Store from the European Centre for Medium-Range Weather Forecasts (ECMWF) and and can be downloaded via https://doi.org/10.24381/cds.bd0915c6 (Hersbach et al., 2023).

Author contributions. The study was designed by TS and supervised by ST. The data processing, analysis, visualization and writing of this study was carried out by TS. ST managed the study and provided extensive support. Both authors also reviewed and proofread this study.

Competing interests. The contact author has declared that none of the authors has any competing interests.

Disclaimer.

Acknowledgements. The Bonn X-band radar (BoXPol) was funded by the German Research Foundation (Deutsche Forschungsgemeinschaft, DFG) within TR32 "Patterns in Soil-Vegetation-Atmosphere Systems". The research was carried out as part of the DFG-funded priority programe SPP-2115 "Polarimetric Radar Observations meet Atmospheric Modelling (PROM, https://www2.meteo.uni-bonn.de/spp2115)"in the project "Climate model PArameterizations informed by RAdar (PARA)". We thank Velibor Pejcic and Ju-Yu Chen for the idea of calibrating Z_H with the reverse Z_H-Z_{DR} method and Velibor Pejcic also for helpful discussions about calibrating ground based radars using satellite (spaceborn-radar) information and provision of satellite data. We also thank Martin Lennefer and Kai Mühlbauer for providing the logbook of BoXPol and careful maintenance of BoXPol over many years. We are also grateful to Kai Mühlbauer with respect to the open-source radar library wradlib https://docs.wradlib.org/en/stable/index.html, last accessed: 27 January 2026) for processing and visualization of radar data.

Financial support. This research has been funded by DFG in the framework of PROM (grant no. TR 1023/15-1).

Appendix A: Shannon information entropy and Melting Layer (ML) detection to identify homogeneous (stratiform) events

The QVP methodology requires nearly homogeneous weather conditions, such that the inherent averaging process results in a significant reduction of the statistical errors (Ryzhkov et al., 2016), quantified e.g. with the standard error of the mean (Von Storch and Zwiers, 2002). Additional variants of the QVP methodology, e.g. range-defined QVPs (RD-QVPs; Tobin and Kumjian, 2017) using all available elevation scans within an inverse distance weighting procedure, or columnar vertical profiles (CVPs; Murphy et al., 2020) also using multiple elevation scans but in limited range and azimuth sectors, have been developed for different applications. However, the required degree of homogeneity or acceptable inhomogeneities, caused e.g. by embed-

https://doi.org/10.5194/egusphere-2026-493
Preprint. Discussion started: 2 March 2026

ded convection or nonuniform beam filling (NBF; e.g. Ryzhkov, 2007; Ryzhkov and Zrnić, 2019, especially for higher antenna beamwidths), has not yet been explored for these methodologies to the authors' knowledge. Instead, rather subjective "by eye" impressions are mostly used.

In order to distinguish between homogeneous (stratiform) and convective events or exclude embedded convection from widespread stratiform rain, an automated and robust method is introduced. It combines ML detection with the Shannon information entropy ($\eta(X)$; Shannon, 1948; Trömel et al., 2023). The latter measures the average degree of uncertainty of the realisations of a random variable. For the sake of simplicity, a normalised version is used. Given a discrete random variable (X) with possible realisations $x_1,\ldots,x_m$ and probabilities $\mathrm{P}(x_1),\ldots,\mathrm{P}(x_m)$, the normalised Shannon information entropy ($\eta(X)_{norm}$) of X is defined as

$$\eta(X)_{norm} = \frac{\eta(X)}{\eta(X)_{max}} = -\frac{1}{\log_{10}(m)} \sum_{k=1}^{m} \mathrm{P}(x_k)\log_{10}(\mathrm{P}(x_k)) = \frac{1}{\log_{10}(m)} \sum_{k=1}^{n} \mathrm{P}(x_k) I(x_k). \tag{A1}$$

In Eq. A1 the maximum possible Shannon information entropy ($\eta(X)_{max}$) follows a uniform distribution with sample size m and $\mathrm{P}(x_k) = 1/m$ with $k = 1,\ldots,m$. $I(x_k)$ denotes the so-called self information (Borda, 2011, e.g.) of individual realisations x_k of X and quantifies the level of "surprise" of a specific event. The higher (smaller) the probability of an event, the less (more) "surprising" it is and therefore $I(x_k)$ is smaller (larger). The probabilities are non-negative $\big(\mathrm{P}(x_k) \geq 0\big)$ and additive $\big(\sum_{k=1}^{m} \mathrm{P}(x_k) = 1$; e.g. Han and Kobayashi, 2002$\big)$. Thus, $\eta(X)$ represents the expected value of the information content of X $\big(\eta(X) = E[I(X)]$; e.g. Borda, 2011$\big)$.

In order to apply Eq. A1 to PPI scans, the $\mathrm{P}(x_k)$ are calculated at each distance (range) over all azimuths, i.e. for a 1° beam width $\mathrm{P}(x_k) = x_k / \sum_{k=1}^{360} x_k$. In this study, the values x_k refer to either Z_H in linear scale ($Z_h = 10^{0.1 Z_H}$), Z_{DR} in linear scale ($Z_{dr} = 10^{0.1 Z_{DR}}$) (unitless), K_{DP} or ρ_{HV} at a certain range at azimuth k. Since Eq. A1 is only defined for positive values, also K_{DP} is limited to values > 0 °km^{-1}. Values of $\eta(X)_{norm}$ close to 1 represent homogeneous conditions while values close to 0 represent inhomogeneous conditions. In this study a threshold of 0.85 is used to identify sufficiently homogeneous stratiform PPIs. The impact of embedded, more convective sectors on $\eta(X)_{norm}$ within an overall stratiform event is illustrated in Fig. A1.

As expected, $\eta(X)_{norm}$ decreases with increasing μ of $\mathcal{N}(\mu,\sigma)$ describing the embedded convection, but also the amount of inserted convective bins has a strong influence . First, $\eta(X)_{norm}$ decreases with increasing number of convective bins (see violet versus blue distribution and grey versus red distribution in Fig. A1), however, if the sample size of convective pixels exceeds a certain fraction of the overall PPI, $\eta(X)_{norm}$ increases again (see yellow distribution) but the PPI is still characterized as inhomogeneous ($\eta(X)_{norm} < 0.85$). For even higher μ (10000 mm^6 m^{-3}; green distribution) $\eta(X)_{norm}$ is decreasing again. Note that the width of the $\eta(X)_{norm}$ distributions narrows with increasing μ of the convective $\mathcal{N}(\mu,\sigma)$ distribution and also with the number of inserted convective bins. This can be attributed to the constant and quite small $\sigma = 500$ mm^6 m^{-3}.

The overall recommended strategy combining ML detection and the Shannon information entropy to identify homogeneous stratiform events is as follows:

https://doi.org/10.5194/egusphere-2026-493
Preprint. Discussion started: 2 March 2026

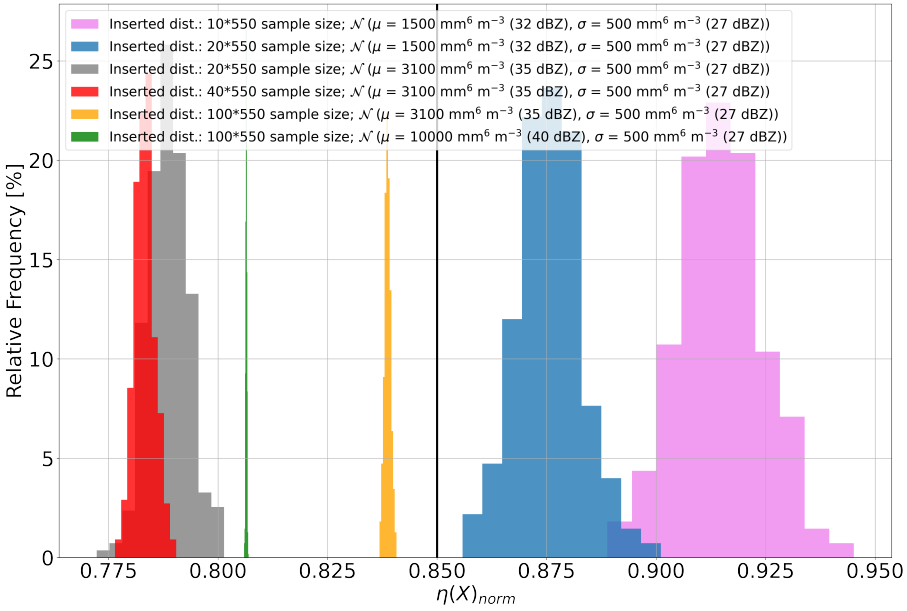

Figure A1. Z_h values of a fictitious PPI scan with 360 azimuths times 550 range bins in stratiform rain are described as a realization of a Gaussian distribution with a mean value of 100 mm^6 m^{-3} and a standard deviation of 10 mm^6 m^{-3} ($\mathcal{N}$ (μ = 100 mm^6 m^{-3} (20 dBZ), σ = 10 mm^6 m^{-3} (10 dBZ))). Embedded convection is introduced by replacing for a certain number of azimuths (e.g., 20, 40, and 100 out of 360) at each distance stratiform Z_h values by the ones generated as a realization of a Gaussian distribution with increased μ values (e.g., 3100 mm^6 m^{-3}) and constant values of σ of 500 mm^6 m^{-3}. For illustration $\eta(X)_{norm}$ is calculated based on these simulated Z_h values only and for different scenarios of embedded convection using Eq. A1. Resulting distributions of $\eta(X)_{norm}$ are shown in violet, blue, grey, red, yellow, and green if embedded convection is introduced with sample size 10*550 following $\mathcal{N}$ (μ = 1500 mm^6 m^{-3} (32 dBZ), σ = 500 mm^6 m^{-3} (27 dBZ)), with sample size 20*550 following $\mathcal{N}$ (μ = 1500 mm^6 m^{-3} (32 dBZ), σ = 500 mm^6 m^{-3} (27 dBZ)), with sample size 20*550 following $\mathcal{N}$ (μ = 3100 mm^6 m^{-3} (35 dBZ), σ = 500 mm^6 m^{-3} (27 dBZ)), with sample size 40*550 following $\mathcal{N}$ (μ = 3100 mm^6 m^{-3} (35 dBZ), σ = 500 mm^6 m^{-3} (27 dBZ)), with sample size 100*550 following $\mathcal{N}$ (μ = 3100 mm^6 m^{-3} (35 dBZ), σ = 500 mm^6 m^{-3} (27 dBZ)), and with sample size 100*550 following $\mathcal{N}$ (μ = 10000 mm^6 m^{-3} (40 dBZ), σ = 500 mm^6 m^{-3} (27 dBZ)), respectively. The black line shows the used threshold in this study series of 0.85 for $\eta(X)_{norm}$.

1. The ML detection of Wolfensberger et al. (2016) adapted to the QVP methodology (Ryzhkov et al., 2016; Trömel et al., 2014) is applied including the estimation of an average K_{DP} within the ML following Trömel et al. (2019) and removal of contributions of backscatter differential phase (δ). No (differential) attenuation correction is applied to the PPIs measured at 18° elevation. Only PPIs with a detected ML are considered as stratiform and enter as candidates for potentially homogeneous PPIs the ensuing analysis steps.

2. Time steps with a detected ML bottom at higher altitudes than ML top are neglected as well as cases with unrealistic heights for the ML top (>10 km).

https://doi.org/10.5194/egusphere-2026-493
Preprint. Discussion started: 2 March 2026

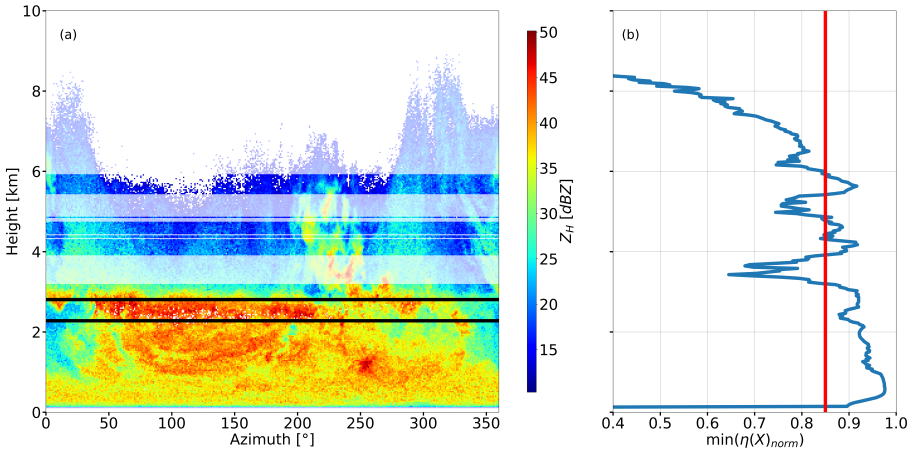

Figure A2. PPI of Z_H in an azimuth-height display (a) monitored with the polarimetric X-band radar in Bonn, BoXPol, on 30 May 2016 at 03:11 UTC. ML top and bottom heights are indicated as black lines and excluded inhomogenous sequences are displayed as transparent regions. The according profile of the minimum normalised Shannon information entropy ($\min(\eta(X)_{norm})$) (b) is shown together the applied threshold for filtering (0.85) as red line.

3. ML top and bottom identified in 2. are treated as first guess estimates and modified to nearby profile locations, where ρ_{HV} returns to values above 0.97 (Giangrande et al., 2008) for better comparability with previous ML statistics as e.g. Trömel et al. (2019).

4. $\eta(X)_{norm}$ is calculated at each range/height over the azimuth dimension as a function of Z_h, Z_{dr}, ρ_{HV} and K_{DP} (without δ contaminations), respectively.

5. If all $\eta(X)_{norm}$ values obtained for the polarimetric variables mentioned in 4. are greater than or equal 0.85, the respective range gates are classified as stratiform and included in the overall stratiform data set. The methodology introduced filters both strong convective inclusions and sequences with a low number of valid measurements, e.g. near the cloud top. Assuming always a full 360° circle in Eq. A1 to determine $\eta(X)_{max}$, regions with only few valid measurements are automatically filtered out via the enhanced $\eta(X)_{max}$ in the denominator of Eq. A1. Note that $\min(\eta(X)_{norm})$ is mainly dominated by changes in Z_h, but any anomalous values inK_{DP}, Z_{dr} or ρ_{HV} can be treated appropriately to obtain the best possible homogeneous (stratiform) data sequences.

6. Finally, using the temperature information from ERA5, heights of the ML top are only allowed at temperatures between -6 and 4 °C, while height levels of the ML bottom are restricted to temperatures between -2 and 8 °C.

Figure A2 illustrates the resulting reduction of $\min(\eta(X)_{norm})$ below the 0.85 threshold due to embedded convection in a measured PPI. Inhomogeneities near the cloud top are filtered out as well.

In summary, tests and simulations showed that the $\min(\eta(X)_{norm})$ threshold of 0.85 used in this study still allows some weaker embedded convective bins within an overall stratiform event (see e.g. the violet and blue distributions in Fig. A1).

https://doi.org/10.5194/egusphere-2026-493
Preprint. Discussion started: 2 March 2026

Depending on requirements, a higher threshold value (e.g. 0.9) for more aggressive filtering, or a weaker threshold value (e.g. 0.8 as in Trömel et al., 2023) for more restrained filtering could be used.

The entropy method can also be applied to different sectors of a PPI or a moving $\min(\eta(X)_{norm})$ with suitable window sizes over the azimuth dimension could be used to identify homoegenous sectors within a PPI, which may in total not show a sufficient degree of homogeneity. Within the RDQVP framework, the method suggested may also identify the most inhomogeneous elevation scans to adjust the threshold value used for the ranges in the inverse distance weighting procedure (for more information see Tobin and Kumjian, 2017).

Furthermore, the so-called permutation entropy (PE; Henry and Judge, 2019; Bandt and Pompe, 2002) could be implemented in future studies. As described above, $\eta(X)$ is positive semidefinite and negative K_{DP} values can't be taken directly into account. Additionally, the typically smaller range of values of Z_{dr}, ρ_{HV} and K_{DP} compared to Z_h reduces the impact of the aforementioned variables on $\min(\eta(X)_{norm})$. However, PE is based on relative frequencies of permutations of partitioned one-dimensional data (on time-series data as shown in Bandt and Pompe, 2002, or applied on radar data, e.g. Z_h values over the azimuth dimension). Thus, by calculating the minimum of the normalized version of PE (PE_{norm}; Henry and Judge, 2019), it is guaranteed that polarimetric variables covering a smaller range of values (see step 5 above, e.g., for ρ_{HV}) may influence the homogeneity estimate to the same extent as those covering a larger range of values.

Appendix B: Validation of the melting layer detection algorithm using ERA5

ML top heights are mostly located below the 0 °C isotherm (e.g. Song et al., 2021; Romatschke, 2021). One possible reason are values of relative humidity with respect to water (RH water) below 100 % favoring sublimation instead of melting (e.g. Heymsfield et al., 2021; Carlin and Ryzhkov, 2019). Thus, the ML top height rather indicates the height of the 0 °C wet-bulb temperature (see e.g. https://glossary.ametsoc.org/wiki/Wet-bulb_temperature). Besides sublimative cooling, faster falling rimed particles with higher density and/or larger aggregates result in a sagging of the ML and typical polarimetric ML (bright band) signatures at lower height levels (e.g. car; Kumjian et al., 2016; Xie et al., 2016).

In order to evaluate the ML detection algorithm, detected ML top heights are compared with both the heights closest to the 0 °C wet-bulb temperature isotherm and environmental temperature isotherm obtained from ERA5 by linearly interpolating from the nearest grid point to the location of BoXPol, as a 2D distribution (see Fig. B1). To ensure a thorough validation, no predefined temperature thresholds are applied (like in step 6 in A1).

The comparison between both height levels indicates a very good agreement. Also, in terms of statistical quantities, the RMSE with 270.40 m, the MAE with 78.14 m, the MB[6] with 171.14 m, and especially the Pearson correlation coefficient of 0.95 demonstrate the reliability of the algorithm. Also, for the environmental 0 °C temperature isotherm, the statistical

[6]The MB is the mean value between the difference of the heights nearest to the 0 °C wet-bulb temperature isotherm calculated from ERA5 temperatures and the detected ML top heights.

https://doi.org/10.5194/egusphere-2026-493
Preprint. Discussion started: 2 March 2026

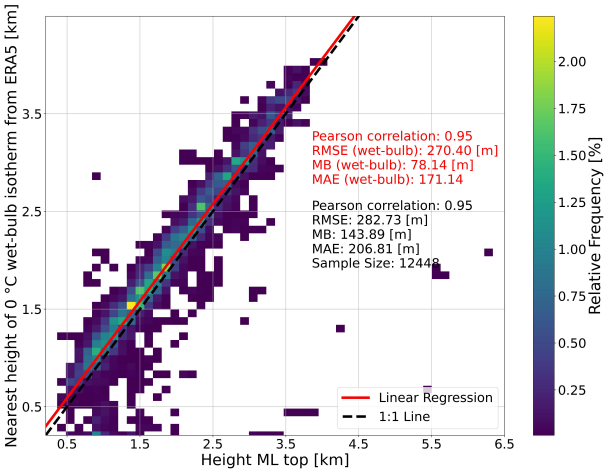

Figure B1. Scatter-density plots of the 0 °C wet-bulb temperature height level from ERA5 versus detected ML top heights. In addition, the Pearson correlation coefficient, RMSE, MB and MAE are given for the comparison of the ML top heights with both, the heights of the 0 °C wet-bulb temperature isotherm (red) and the 0 °C environmental temperature isotherm (black).

quantities show only slightly higher values and in line with e.g. Song et al. (2021), their figure 6. Uncertainties may arise due to the interpolation process from the temporally coarser grid of ERA5 (1 h) and intrinsic uncertainties.

https://doi.org/10.5194/egusphere-2026-493
Preprint. Discussion started: 2 March 2026

References

Atlas, D.: Radar calibration: Some simple approaches, Bulletin of the American Meteorological Society, 83, 1313–1316, https://doi.org/10.1175/1520-0477-83.9.1313, 2002.

Atlas, D. and Mossop, S.: Calibration of a weather radar by using a standard target, Bulletin of the American Meteorological Society, 41, 377–382, https://doi.org/10.1175/1520-0477-41.7.377, 1960.

Bandt, C. and Pompe, B.: Permutation entropy: a natural complexity measure for time series, Physical Review Letters, 88, 174 102, https://doi.org/10.1103/PhysRevLett.88.174102, 2002.

Blahak, U.: RADAR_MIE_LM and RADAR_MIELIB — Calculation of Radar Reflectivity from Model Output, Technical Report 28, Consortium for Small Scale Modeling (COSMO), https://doi.org/10.5676/DWD_pub/nwv/cosmo-tr_28, 2016.

Blahak, U. and de Lozar, A.: EMVORADO — Efficient Modular VOlume scan RADar Operator. A User's Guide, Deutscher Wetterdienst, www.cosmo-model.org/content/model/documentation/core/emvorado_userguide.pdf, 2021.

Blanke, A., Gergely, M., and Trömel, S.: A new aggregation and riming discrimination algorithm based on polarimetric weather radars, Atmospheric Chemistry and Physics, 25, 4167–4184, https://doi.org/10.5194/acp-25-4167-2025, 2025.

Borda, M.: Fundamentals in information theory and coding, Springer Science & Business Media, https://doi.org/10.1007/978-3-642-20347-3, 2011.

Brandes, E. A., Zhang, G., and Vivekanandan, J.: Experiments in rainfall estimation with a polarimetric radar in a subtropical environment, Journal of Applied Meteorology and Climatology, 41, 674–685, https://doi.org/10.1175/1520-0450(2002)041<0674:EIREWA>2.0.CO;2, 2002.

Carlin, J. T. and Ryzhkov, A. V.: Estimation of melting-layer cooling rate from dual-polarization radar: Spectral bin model simulations, Journal of Applied Meteorology and Climatology, 58, 1485–1508, https://doi.org/10.1175/JAMC-D-18-0343.1, 2019.

Chen, J.-Y., Trömel, S., Ryzhkov, A., and Simmer, C.: Assessing the benefits of specific attenuation for quantitative precipitation estimation with a C-band radar network, Journal of Hydrometeorology, 22, 2617–2631, https://doi.org/10.1175/JHM-D-20-0299.1, 2021.

Chu, Z., Liu, W., Zhang, G., Kou, L., and Li, N.: Continuous monitoring of differential reflectivity bias for C-band polarimetric radar using online solar echoes in volume scans, Remote Sensing, 11, 2714, https://doi.org/10.3390/rs11222714, 2019.

Crisologo, I.: Using spaceborne radar platforms to enhance the homogeneity of weather radar calibration, Ph.D. thesis, Universität Potsdam, https://publishup.uni-potsdam.de/frontdoor/index/index/docId/44570, 2019.

Crisologo, I., Warren, R. A., Mühlbauer, K., and Heistermann, M.: Enhancing the consistency of spaceborne and ground-based radar comparisons by using beam blockage fraction as a quality filter, Atmospheric Measurement Techniques, 11, 5223–5236, https://doi.org/10.5194/amt-11-5223-2018, 2018.

Diederich, M., Ryzhkov, A., Simmer, C., Zhang, P., and Trömel, S.: Use of specific attenuation for rainfall measurement at X-band radar wavelengths. Part I: Radar calibration and partial beam blockage estimation, Journal of Hydrometeorology, 16, 487–502, https://doi.org/10.1175/JHM-D-14-0066.1, 2015.

Doms, G. and Baldauf, M.: A Description of the Nonhydrostatic Regional COSMO-Model LM. Part I: Dynamics and Numerics, Consortium for Smallscale Modeling (COSMO), https://doi.org/10.5676/DWD_pub/nwv/cosmo-doc_5.05_I, 2018.

https://doi.org/10.5194/egusphere-2026-493
Preprint. Discussion started: 2 March 2026

Doms, G., Förstner, J., Heise, E., Herzog, H.-J., Mironov, D., Raschendorfer, M., Reinhardt, T., Ritter, B., Schrodin, R., Schulz, J.-P., and Vogel, G.: A Description of the Nonhydrostatic Regional COSMO-Model. Part II: Physical Parameterization, Consortium for Smallscale Modeling (COSMO), https://doi.org/10.5676/DWD_pub/nwv/cosmo-doc_5.05_II, 2018.

Doviak, R. J., Zrnic, D. S., and Schotland, R. M.: Doppler radar and weather observations, Applied Optics, 33, 4531, 1994.

Fan, J., Han, B., Varble, A., Morrison, H., North, K., Kollias, P., Chen, B., Dong, X., Giangrande, S. E., Khain, A., Lin, Y., Mansell, E., Milbrandt, J. A., Stenz, R., Thompson, G., and Wang, Y.: Cloud-resolving model intercomparison of an MC3E squall line case: Part I—Convective updrafts, Journal of Geophysical Research: Atmospheres, 122, 9351–9378, https://doi.org/10.1002/2017JD026622, 2017.

Frech, M.: 9B. 3 Monitoring the data quality of the new polarimetric weather radar network of the German Meteorological Service, https://ams.confex.com/ams/36Radar/webprogram/Paper228472.html, 2013.

Frech, M. and Hubbert, J.: Monitoring the differential reflectivity and receiver calibration of the German polarimetric weather radar network, Atmospheric Measurement Techniques, 13, 1051–1069, https://doi.org/10.5194/amt-13-1051-2020, 2020.

Frech, M., Hagen, M., and Mammen, T.: Monitoring the absolute calibration of a polarimetric weather radar, Journal of Atmospheric and Oceanic Technology, 34, 599–615, https://doi.org/10.1175/JTECH-D-16-0076.1, 2017.

Fridlind, A. M., Li, X., Wu, D., van Lier-Walqui, M., Ackerman, A. S., Tao, W.-K., McFarquhar, G. M., Wu, W., Dong, X., Wang, J., Ryzhkov, A., Zhang, P., Poellot, M. R., Neumann, A., and Tomlinson, J. M.: Derivation of aerosol profiles for MC3E convection studies and use in simulations of the 20 May squall line case, Atmospheric Chemistry and Physics, 17, 5947–5972, https://doi.org/10.5194/acp-17-5947-2017, 2017.

Gabella, M.: On the use of bright scatterers for monitoring Doppler, dual-polarization weather radars, Remote Sensing, 10, 1007, https://doi.org/10.3390/rs10071007, 2018.

Giangrande, S. E., Krause, J. M., and Ryzhkov, A. V.: Automatic designation of the melting layer with a polarimetric prototype of the WSR-88D radar, Journal of Applied Meteorology and Climatology, 47, 1354–1364, https://doi.org/10.1175/2007JAMC1634.1, 2008.

Gorgucci, E., Scarchilli, G., and Chandrasekar, V.: Calibration of radars using polarimetric techniques, IEEE Transactions on Geoscience and Remote Sensing, 30, 853–858, https://doi.org/10.1109/36.175319, 1992.

Gorgucci, E., Baldini, L., and Chandrasekar, V.: What is the shape of a raindrop? An answer from radar measurements, Journal of the Atmospheric Sciences, 63, 3033–3044, https://doi.org/10.1175/JAS3781.1, 2006.

Gourley, J. J., Illingworth, A. J., and Tabary, P.: Absolute calibration of radar reflectivity using redundancy of the polarization observations and implied constraints on drop shapes, Journal of Atmospheric and Oceanic Technology, 26, 689–703, https://doi.org/10.1175/2008JTECHA1152.1, 2009.

Griffin, E. M., Schuur, T. J., and Ryzhkov, A. V.: A polarimetric analysis of ice microphysical processes in snow, using quasi-vertical profiles, Journal of Applied Meteorology and Climatology, 57, 31–50, https://doi.org/10.1175/JAMC-D-17-0033.1, 2018.

Han, T. S. and Kobayashi, K.: Mathematics of Information and Coding, vol. 203, American Mathematical Society, 2002.

Henry, M. and Judge, G.: Permutation entropy and information recovery in nonlinear dynamic economic time series, Econometrics, 7, 10, https://doi.org/10.3390/econometrics7010010, 2019.

Hersbach, H., Bell, B., Berrisford, P., Hirahara, S., Horányi, A., Muñoz-Sabater, J., Nicolas, J., Peubey, C., Radu, R., Schepers, D., et al.: The ERA5 global reanalysis, Quarterly Journal of the Royal Meteorological Society, 146, 1999–2049, https://doi.org/10.1002/qj.3803, 2020.

Hersbach, H., Bell, B., Berrisford, P., Biavati, G., Horányi, A., Muñoz Sabater, J., Nicolas, J., Peubey, C., Radu, R., Rozum, I., Schepers, D., Simmons, A., Soci, C., Dee, D., and Thépaut, J.-N.: ERA5 hourly data on pressure levels from 1940 to present, Copernicus Climate Change Service (C3S) Climate Data Store (CDS), https://doi.org/10.24381/cds.bd0915c6, 2023.

https://doi.org/10.5194/egusphere-2026-493
Preprint. Discussion started: 2 March 2026

Heymsfield, A. J., Bansemer, A., Theis, A., and Schmitt, C.: Survival of snow in the melting layer: Relative humidity influence, Journal of the Atmospheric Sciences, 78, 1823–1845, https://doi.org/10.1175/JAS-D-20-0353.1, 2021.

Holleman, I., Huuskonen, A., Gill, R., and Tabary, P.: Operational monitoring of radar differential reflectivity using the sun, Journal of Atmospheric and Oceanic Technology, 27, 881–887, https://doi.org/10.1175/2010JTECHA1381.1, 2010.

Holoborodko, P.: Low-noise Lanczos differentiators, Online resource, https://www.holoborodko.com/pavel/numerical-methods/numerical-derivative/lanczos-low-noise-differentiators/, 2015.

Hou, A. Y., Kakar, R. K., Neeck, S., Azarbarzin, A. A., Kummerow, C. D., Kojima, M., Oki, R., Nakamura, K., and Iguchi, T.: The global precipitation measurement mission, Bulletin of the American Meteorological Society, 95, 701–722, https://doi.org/10.1175/BAMS-D-13-00164.1, 2014.

Houze Jr, R. A., Brodzik, S., Schumacher, C., Yuter, S. E., and Williams, C. R.: Uncertainties in oceanic radar rain maps at Kwajalein and implications for satellite validation, Journal of Applied Meteorology and Climatology, 43, 1114–1132, https://doi.org/10.1175/1520-0450(2004)043<1114:UIORRM>2.0.CO;2, 2004.

Hu, J., Ryzhkov, A., and Dunnavan, E. L.: Vertical profile climatology of polarimetric radar variables and retrieved microphysical parameters in synoptic and lake effect snowstorms, Journal of Geophysical Research: Atmospheres, 129, e2024JD041318, https://doi.org/10.1029/2024JD041318, 2024.

Hunzinger, A., Hardin, J. C., Bharadwaj, N., Varble, A., and Matthews, A.: An extended radar relative calibration adjustment (eRCA) technique for higher-frequency radars and range–height indicator (RHI) scans, Atmospheric Measurement Techniques, 13, 3147–3166, https://doi.org/10.5194/amt-13-3147-2020, 2020.

Kennedy, P. C. and Rutledge, S. A.: S-band dual-polarization radar observations of winter storms, Journal of Applied Meteorology and Climatology, 50, 844–858, https://doi.org/10.1175/2010JAMC2558.1, 2011.

Kumjian, M. R.: Principles and Applications of Dual-Polarization Weather Radar. Part I: Description of the Polarimetric Radar Variables., Journal of Operational Meteorology, 1, https://doi.org/10.15191/nwajom.2013.0119, 2013a.

Kumjian, M. R.: Principles and Applications of Dual-Polarization Weather Radar. Part III: Artifacts., Journal of Operational Meteorology, 1, https://doi.org/10.15191/nwajom.2013.0121, 2013b.

Kumjian, M. R. and Ryzhkov, A. V.: The impact of evaporation on polarimetric characteristics of rain: Theoretical model and practical implications, Journal of Applied Meteorology and Climatology, 49, 1247–1267, https://doi.org/10.1175/2010JAMC2243.1, 2010.

Kumjian, M. R. and Ryzhkov, A. V.: The Impact of Size Sorting on the Polarimetric Radar Variables, Journal of the Atmospheric Sciences, 69, 2042–2060, https://doi.org/10.1175/JAS-D-11-0125.1, 2012.

Kumjian, M. R., Mishra, S., Giangrande, S. E., Toto, T., Ryzhkov, A. V., and Bansemer, A.: Polarimetric radar and aircraft observations of saggy bright bands during MC3E, Journal of Geophysical Research: Atmospheres, 121, 3584–3607, https://doi.org/10.1002/2015JD024446, 2016.

Le Loh, J., Chang, W.-Y., Hsu, H.-W., Lin, P.-F., Chang, P.-L., Teng, Y.-L., and Liou, Y.-C.: Long-term assessment of the reflectivity biases and wet-radome effect using collocated operational s-and c-band dual-polarization radars, IEEE Transactions on Geoscience and Remote Sensing, 60, 1–17, https://doi.org/10.1109/TGRS.2022.3170609, 2022.

Lee, J.-E., Kwon, S., and Jung, S.-H.: Real-Time Calibration and Monitoring of Radar Reflectivity on Nationwide Dual-Polarization Weather Radar Network, Remote Sensing, 13, 2936, https://doi.org/10.3390/rs13152936, 2021.

Louf, V. and Protat, A.: Real-time monitoring of weather radar network calibration and antenna pointing, Journal of Atmospheric and Oceanic Technology, 40, 823–844, https://doi.org/10.1175/JTECH-D-22-0118.1, 2023.

https://doi.org/10.5194/egusphere-2026-493
Preprint. Discussion started: 2 March 2026

Louf, V., Protat, A., Warren, R. A., Collis, S. M., Wolff, D. B., Raunyiar, S., Jakob, C., and Petersen, W. A.: An integrated approach to weather radar calibration and monitoring using ground clutter and satellite comparisons, Journal of Atmospheric and Oceanic Technology, 36, 17–39, https://doi.org/10.1175/JTECH-D-18-0007.1, 2019.

Marks, D. A., Wolff, D. B., Carey, L. D., and Tokay, A.: Quality control and calibration of the dual-polarization radar at Kwajalein, RMI, Journal of Atmospheric and Oceanic Technology, 28, 181–196, https://doi.org/10.1175/2010JTECHA1462.1, 2011.

Masaki, T., Iguchi, T., Kanemaru, K., Furukawa, K., Yoshida, N., Kubota, T., and Oki, R.: Calibration of the dual-frequency precipitation radar onboard the Global Precipitation Measurement Core Observatory, IEEE Transactions on Geoscience and Remote Sensing, 60, 1–16, https://doi.org/10.1109/TGRS.2020.3039978, 2020.

Murphy, A. M., Ryzhkov, A., and Zhang, P.: Columnar vertical profile (CVP) methodology for validating polarimetric radar retrievals in ice using in situ aircraft measurements, Journal of Atmospheric and Oceanic Technology, 37, 1623–1642, https://doi.org/10.1175/JTECH-D-20-0011.1, 2020.

Ori, D., Schemann, V., Karrer, M., Dias Neto, J., von Terzi, L., Seifert, A., and Kneifel, S.: Evaluation of ice particle growth in ICON using statistics of multi-frequency Doppler cloud radar observations, Quarterly Journal of the Royal Meteorological Society, 146, 3830–3849, https://doi.org/10.1002/qj.3875, 2020.

Pejcic, V., Saavedra Garfias, P., Mühlbauer, K., Trömel, S., and Simmer, C.: Comparison between precipitation estimates of ground-based weather radar composites and GPM's DPR rainfall product over Germany, Meteorologische Zeitschrift, https://doi.org/10.1127/metz/2020/1039, 2020.

Pejcic, V., Soderholm, J., Mühlbauer, K., Louf, V., and Trömel, S.: Five years calibrated observations from the University of Bonn X-band weather radar (BoXPol), Scientific Data, 9, 1–9, https://doi.org/10.1038/s41597-022-01656-0, 2022.

Planat, N., Gehring, J., Vignon, É., and Berne, A.: Identification of snowfall microphysical processes from Eulerian vertical gradients of polarimetric radar variables, Atmospheric Measurement Techniques, 14, 4543–4564, https://doi.org/10.5194/amt-14-4543-2021, 2021.

Protat, A., Louf, V., Soderholm, J., Brook, J., and Ponsonby, W.: Three-way calibration checks using ground-based, ship-based, and space-borne radars, Atmospheric Measurement Techniques, 15, 915–926, https://doi.org/10.5194/amt-15-915-2022, 2022.

Richardson, L. M., Cunningham, J. G., Zittel, W. D., Lee, R. R., Ice, R. L., Melnikov, V. M., Hoban, N. P., and Gebauer, J. G.: Bragg scatter detection by the WSR-88D. Part I: Algorithm development, Journal of Atmospheric and Oceanic Technology, 34, 465–478, https://doi.org/10.1175/JTECH-D-16-0030.1, 2017.

Rinehart, R. E.: Radar for Meteorologists, Rinehart Publications, 3 edn., 1997.

Romatschke, U.: Melting layer detection and observation with the NCAR airborne W-band radar, Remote Sensing, 13, 1660, https://doi.org/10.3390/rs13091660, 2021.

Ryzhkov, A., Pinsky, M., Pokrovsky, A., and Khain, A.: Polarimetric radar observation operator for a cloud model with spectral microphysics, Journal of Applied Meteorology and Climatology, 50, 873–894, https://doi.org/10.1175/2010JAMC2363.1, 2011.

Ryzhkov, A., Zhang, P., Reeves, H., Kumjian, M., Tschallener, T., Trömel, S., and Simmer, C.: Quasi-vertical profiles—A new way to look at polarimetric radar data, Journal of Atmospheric and Oceanic Technology, 33, 551–562, https://doi.org/10.1175/JTECH-D-15-0020.1, 2016.

Ryzhkov, A. V.: The impact of beam broadening on the quality of radar polarimetric data, Journal of Atmospheric and Oceanic Technology, 24, 729–744, https://doi.org/10.1175/JTECH2003.1, 2007.

Ryzhkov, A. V. and Zrnić, D. S.: Radar polarimetry for weather observations, vol. 486, Springer, https://doi.org/10.1007/978-3-030-05093-1, 2019.

https://doi.org/10.5194/egusphere-2026-493
Preprint. Discussion started: 2 March 2026

Ryzhkov, A. V., Giangrande, S. E., Melnikov, V. M., and Schuur, T. J.: Calibration issues of dual-polarization radar measurements, Journal of Atmospheric and Oceanic Technology, 22, 1138–1155, https://doi.org/10.1175/JTECH1772.1, 2005.

Ryzhkov, A. V., Snyder, J., Carlin, J. T., Khain, A., and Pinsky, M.: What polarimetric weather radars offer to cloud modelers: forward radar operators and microphysical/thermodynamic retrievals, Atmosphere, 11, 362, https://doi.org/10.3390/atmos11040362, 2020.

Sanchez-Rivas, D. and Rico-Ramirez, M. A.: Calibration of radar differential reflectivity using quasi-vertical profiles, Atmospheric Measurement Techniques, 15, 503–520, https://doi.org/10.5194/amt-15-503-2022, 2022.

Schneebeli, M., Leuenberger, A., Frech, M., and Ventura, J.: Weather radar data calibration and monitoring, Advances in Weather Radar, 2, 41–97, https://doi.org/10.1049/SBRA557G_ch2, 2024.

Seifert, A. and Beheng, K. D.: A two-moment cloud microphysics parameterization for mixed-phase clouds. Part 1: Model description, Meteorology and Atmospheric Physics, 92, 45–66, https://doi.org/10.1007/s00703-005-0112-4, 2006.

Shannon, C. E.: A mathematical theory of communication, The Bell System Technical Journal, 27, 379–423, https://doi.org/10.1002/j.1538-7305.1948.tb01338.x, 1948.

Shrestha, P., Mendrok, J., Pejcic, V., Trömel, S., Blahak, U., and Carlin, J. T.: Evaluation of the COSMO model (v5.1) in polarimetric radar space – impact of uncertainties in model microphysics, retrievals and forward operators, Geoscientific Model Development, 15, 291–313, https://doi.org/10.5194/gmd-15-291-2022, 2022.

Silberstein, D. S., Wolff, D. B., Marks, D. A., Atlas, D., and Pippitt, J. L.: Ground clutter as a monitor of radar stability at Kwajalein, RMI, Journal of Atmospheric and Oceanic Technology, 25, 2037–2045, https://doi.org/10.1175/2008JTECHA1063.1, 2008.

Song, J. I., Yum, S. S., Park, S.-H., Kim, K.-H., Park, K.-J., and Joo, S.-W.: Climatology of melting layer heights estimated from cloud radar observations at various locations, Journal of Geophysical Research: Atmospheres, 126, e2021JD034 816, https://doi.org/10.1029/2021JD034816, 2021.

Tobin, D. M. and Kumjian, M. R.: Polarimetric radar and surface-based precipitation-type observations of ice pellet to freezing rain transitions, Weather and Forecasting, 32, 2065–2082, https://doi.org/10.1175/WAF-D-17-0054.1, 2017.

Trömel, S., Ryzhkov, A. V., Zhang, P., and Simmer, C.: Investigations of Backscatter Differential Phase in the Melting Layer, Journal of Applied Meteorology and Climatology, 53, https://doi.org/10.1175/JAMC-D-14-0050.1, 2014.

Trömel, S., Ryzhkov, A. V., Hickman, B., Mühlbauer, K., and Simmer, C.: Polarimetric Radar Variables in the Layers of Melting and Dendritic Growth at X Band—Implications for a Nowcasting Strategy in Stratiform Rain, Journal of Applied Meteorology and Climatology, 58, 2497–2522, https://doi.org/10.1175/JAMC-D-19-0056.1, 2019.

Trömel, S., Simmer, C., Blahak, U., Blanke, A., Doktorowski, S., Ewald, F., Frech, M., Gergely, M., Hagen, M., Janjic, T., Kalesse-Los, H., Kneifel, S., Knote, C., Mendrok, J., Moser, M., Köcher, G., Mühlbauer, K., Myagkov, A., Pejcic, V., Seifert, P., Shrestha, P., Teisseire, A., von Terzi, L., Tetoni, E., Vogl, T., Voigt, C., Zeng, Y., Zinner, T., and Quaas, J.: Overview: Fusion of radar polarimetry and numerical atmospheric modelling towards an improved understanding of cloud and precipitation processes, Atmospheric Chemistry and Physics, 21, https://doi.org/10.5194/acp-21-17291-2021, 2021.

Trömel, S., Blahak, U., Evaristo, R., Mendrok, J., Neef, L., Pejcic, V., Scharbach, T., Shrestha, P., and Simmer, C.: Fusion of radar polarimetry and atmospheric modeling, in: Advances in Weather Radar, Volume 2: Precipitation science, scattering and processing algorithms, The Institution of Engineering and Technology (IET), https://doi.org/10.1049/SBRA557G_ch7, 2023.

Von Storch, H. and Zwiers, F. W.: Statistical Analysis in Climate Research, Cambridge University Press, 2002.

https://doi.org/10.5194/egusphere-2026-493
Preprint. Discussion started: 2 March 2026

Vulpiani, G., Montopoli, M., Passeri, L. D., Gioia, A. G., Giordano, P., and Marzano, F. S.: On the use of dual-polarized C-band radar for operational rainfall retrieval in mountainous areas, Journal of Applied Meteorology and Climatology, 51, 405–425, https://doi.org/10.1175/JAMC-D-10-05024.1, 2012.

Warren, R. A., Protat, A., Siems, S. T., Ramsay, H. A., Louf, V., Manton, M. J., and Kane, T. A.: Calibrating ground-based radars against TRMM and GPM, Journal of Atmospheric and Oceanic Technology, 35, 323–346, https://doi.org/10.1175/JTECH-D-17-0128.1, 2018.

Warren, R. A., Ramsay, H. A., Siems, S. T., Manton, M. J., Peter, J. R., Protat, A., and Pillalamarri, A.: Radar-based climatology of damaging hailstorms in Brisbane and Sydney, Australia, Quarterly Journal of the Royal Meteorological Society, 146, 505–530, https://doi.org/10.1002/qj.3693, 2020.

Waterman, P. C.: Symmetry, unitarity, and geometry in electromagnetic scattering, Physical review D, 3, 825, https://doi.org/10.1103/PhysRevD.3.825, 1971.

Williams, E., Hood, K., Cho, J. Y. N., Smalley, D. J., Sandifer, J. B., Zrnić, D., Melnikov, V. M., Burgess, D. W., Forsyth, D., Webster, T. M., et al.: End-to-end calibration of NEXRAD differential reflectivity with metal spheres, in: Proceedings of the 36th Conference on Radar Meteorology, American Meteorological Society, Breckenridge, Colorado, USA, https://ams.confex.com/ams/36Radar/webprogram/Paper228796.html, 16–20 September 2013, 2013.

Wolfensberger, D., Scipion, D., and Berne, A.: Detection and characterization of the melting layer based on polarimetric radar scans, Quarterly Journal of the Royal Meteorological Society, 142, 108–124, https://doi.org/10.1002/qj.2672, 2016.

Wolff, D. B., Marks, D. A., and Petersen, W. A.: General application of the relative calibration adjustment (RCA) technique for monitoring and correcting radar reflectivity calibration, Journal of Atmospheric and Oceanic Technology, 32, 496–506, https://doi.org/10.1175/JTECH-D-13-00185.1, 2015.

Xie, X., Evaristo, R., Simmer, C., Handwerker, J., and Trömel, S.: Precipitation and microphysical processes observed by three polarimetric X-band radars and ground-based instrumentation during HOPE, Atmospheric Chemistry and Physics, 16, 7105–7116, https://doi.org/10.5194/acp-16-7105-2016, 2016.

Xie, X., Shrestha, P., Mendrok, J., Carlin, J., Trömel, S., and Blahak, U.: Bonn Polarimetric Radar forward Operator (B-PRO), https://doi.org/10.5880/TR32DB.41, 2021.

Ye, F., Wang, X., Li, L., Chen, Y., Lei, Y., Yu, H., Yin, J., Shi, L., Yang, Q., and Huang, Z.: Weather radar calibration method based on UAV-suspended metal sphere, Sensors (Basel, Switzerland), 24, 4611, https://doi.org/10.3390/s24144611, 2024.

Zeng, Y., Blahak, U., and Jerger, D.: An efficient modular volume-scanning radar forward operator for NWP models: description and coupling to the COSMO model, Quarterly Journal of the Royal Meteorological Society, 142, 3234–3256, https://doi.org/10.1002/qj.2904, 2016.

Zittel, W. D., Cunningham, J. G., Lee, R. R., Richardson, L. M., Ice, R. L., and Melnikov, V.: Use of hydrometeors, Bragg scatter, and sun spikes to determine system ZDR biases in the WSR-88D fleet, in: Extended Abstracts of the Eighth European Conference on Radar in Meteorology and Hydrology (ERAD 2014), vol. 12, Garmisch-Partenkirchen, Germany, https://www.pa.op.dlr.de/erad2014/programme/ExtendedAbstracts/132_Zittel.pdf, 2014.